MAGNETIC DOMAIN WALL DYNAMICS IN THE PRESENCE OF AN IN-PLANE FIELD

Thesis by

Kadri L. Vural

In Partial Fulfillment of the Requirements

for the Degree of

Doctor of Philosophy

California Institute of Technology

Pasadena, California

1980

(Submitted May 5, 1980)

to my Mother

and

to the Zinns

ACKNOWLEDGEMENTS

I would like to thank Professor Floyd B. Humphrey for his encouragement, guidance and assistance throughout the course of this work. I would also like to thank Professor Charles H. Wilts, Dr. Laslo Gal, Dr. Tim Gallagher, Dr. Kochan Ju, Dr. Tsutomu Kobayashi, Dr. Bruce E. MacNeal and Dr. George Zimmer for many helpful discussions. Financial assistance from California Institute of Technology and the National Science Foundation is acknowledged. I would like to thank Mrs. Vere Snell for her assistance in typing the text. Finally I express my gratitude and deep appreciation to the Zinns for their encouragement and guidance during my stay at Caltech.

ABSTRACT

The purpose of this work is to understand the domain wall dynamics in the presence of high drive fields and in-plane fields in magnetic bubble materials. Bubble radial expansion method is used to investigate the non-linear region. Saturation velocity is found at low in-plane fields and a drive dependent region at higher in-plane fields. The in-plane field increases all the velocities. There is velocity anisotropy and the wall along the in-plane field generally has a higher velocity than the one normal to it. The domain wall is dynamically deformed through the thickness at high drive and in-plane fields. This deformation is studied in the bulk of the film by transmission (Faraday) mode and at the surfaces by reflection (Kerr) mode. The mechanism for the deformation is based on the spatial variations of the effective in-plane field through the thickness. This causes different parts of the wall to move with different velocities resulting in a deformed wall. The characteristics of the deformed wall are studied in detail for several samples.

TABLE OF CONTENTS

CHAPTER 1

1.1 Bubble Domain Basics

A magnetic domain in a material exhibiting a spontaneous magnetic moment is defined as a region where the magnetization of the material is aligned in the same direction. Two of the simplest domain shapes that exist statically in magnetic bubble materials are shown in Fig. (1.1). An isolated stripe domain with no externally applied field is shown in Fig. (1.1a). In the figure the arrows represent the direction of the local moments. An anisotropy axis exists in a direction normal to the sample plane keeping the moments aligned parallel to it. Stripe domains are usually very long with random maze-like shapes with no external field applied to the sample. The width of the stripes magnetized in one direction is essentially the same as those magnetized in the opposite direction. The area of the stripes with moments pointing down in the figure is equal to the area of the stripes in the rest of the material with moments pointing up. The resultant moment is zero and the material is magnetically neutral. This so-called demagnetized state of the material is where the total energy is minimum. The ends of the stripe may be free or they may extend to the

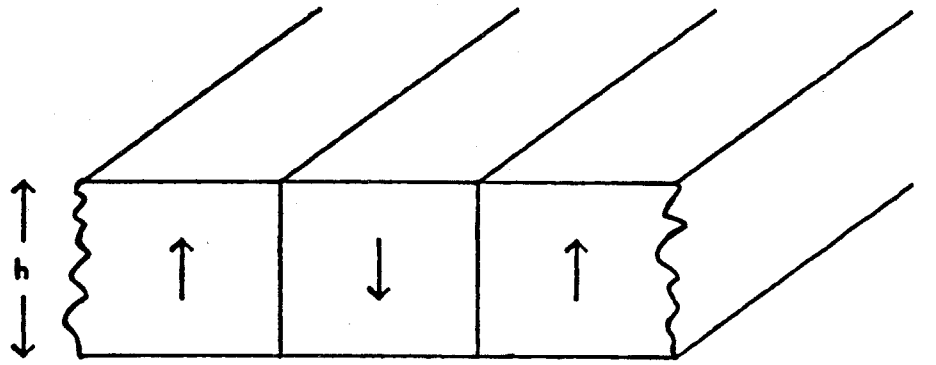

(a)

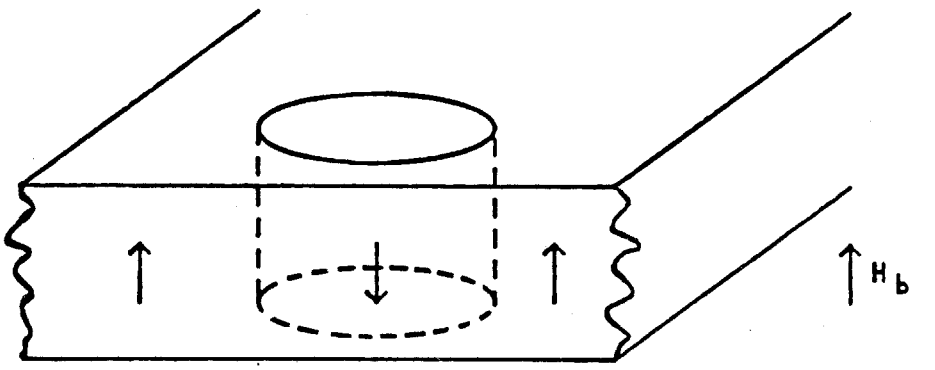

(b)

Fig. 1.1. Schematic of domain configurations in bubble material (a) isolated stripe domain with no applied field (b) isolated bubble domain with applied field H_b normal to the film. An anisotropy exists whose axis is in a direction normal to the plane of the sample.

sides of the sample where they will usually be pinned. When an external field is applied along the direction of the anisotropy and slowly increased, the stripes that are magnetized in the direction opposite to the field first narrow and then, provided the stripe ends are free, shorten. Eventually, when the field is so high that the material is nearly saturated, the stripes with the free ends will become cylindrically shaped domains. This shape domain is called a bubble domain. It is shown in Fig. (1.1b). A bubble domain is a cylindrical region with all the local moments inside aligned opposite to the applied field necessary for its existence while the rest of the material is aligned with the field. Bubble domains, then, are stable only in the presence of an applied field since they exist when the material is almost saturated. Their diameter is about equal to the material thickness which is, in typical materials, a few microns.

The exact size of a bubble is dependent upon the magnitude of the uniform applied field called the bias field[1-4]. As the bias field increases the bubble radius decreases. If the field is high enough the bubble is no longer stable and disappears. This maximum field is called the collapse field and the corresponding radius is called the collapse

radius. When the bias field is decreased the bubble radius increases until a certain field where it expands into a stripe domain. This is called the stripe-out field. This stability range for bubbles between collapse and stripe-out is typically 15 Oe depending on the material parameters.

The bubble domain can be moved isotropically in the material by using local field gradients [3-5]. When the bias field is non-uniform and not symmetrical with respect to the center of the bubble, the bubble will experience a net unbalanced force due to the different values of bias field at each point of the circumference. This unbalanced force causes the bubble to move as an entity in the direction of the net force which will be toward the lower field. For example when a linear field gradient is applied, the bubble will move in the direction of decreasing bias field where it will have a lower energy. Local field gradients can be obtained from current loops on the surface of the material or from another piece of magnetic material in close proximity. This latter method forms the basis for computer memory devices.

1.2 Bubble Devices

Local field gradients of magnitude sufficient to con-

fine and propagate a bubble can be obtained by applying a uniform in-plane magnetic field to a structured magnetic overlay. Permalloy material [6,7] is popular for such overlays. Permalloy is a ferromagnetic material composed of iron-nickel alloy (typically 80% Ni). It has a high permeability at low applied fields and is essentially isotropic in the plane of the material. The magnetization is confined to the plane of the sample by magnetostatic forces since permalloy is highly magnetic. In a bubble device the permalloy is used to transform the uniform in-plane field into a local bias field gradient on the bubble. Conceptually, the mechanism of this transform can be understood by considering a small bar of permalloy parallel to the plane of the bubble material and slightly removed from it. The stray fields from the permalloy will locally modulate the uniform bias field that is always supplied to keep the bubble stable. At one end of the permalloy, in the plane of the bubble, the field will add to the bias whereas at the other end it will subtract. A gradient will be formed which will cause the bubble to move to the end where the resultant field, bias field plus stray field, is the lowest. This place is also the position of lowest energy so that the bubble is stable in this potential well. By arranging the permalloy bars in a periodic pattern and rotating the in-plane field, a

changing local gradient can be obtained and used to achieve bubble propagation.

One of the earliest and most illustrative propagation structures for a shift register in a bubble device is the T and I bar overlay [5]. A schematic top view of this overlay is shown in Fig. (1.2). Although this specific structure is not used in high performance devices any more, it is excellent for illustrating bubble propagation. The dimensions of the I bars are typically 24x4 microns and 0.5 microns thick. They are spaced slightly ($\sim$ 0.7 microns) away from the garnet layer using a SiO_2 layer in-between. When an in-plane field is applied, the long permalloy bars are magnetized in the direction of the field generating a potential well below the bar. The direction of the in-plane field is shown by the arrows on the lefthand side of the figure. Initially (Case A) the in-plane field is in the -y direction with the bubble at the bottom of the I bar where it is stable. When the in-plane field is rotated $\pi/2$ to the -x direction (Case B) the position of the potential well is shifted to the left side of the T bar and the bubble moves to that location. As the in-plane field rotates to the y direction (Case C) the bubble moves to the center of the T bar. Of course, there is another potential well at the far end of the I bar but the one at the top of the T is

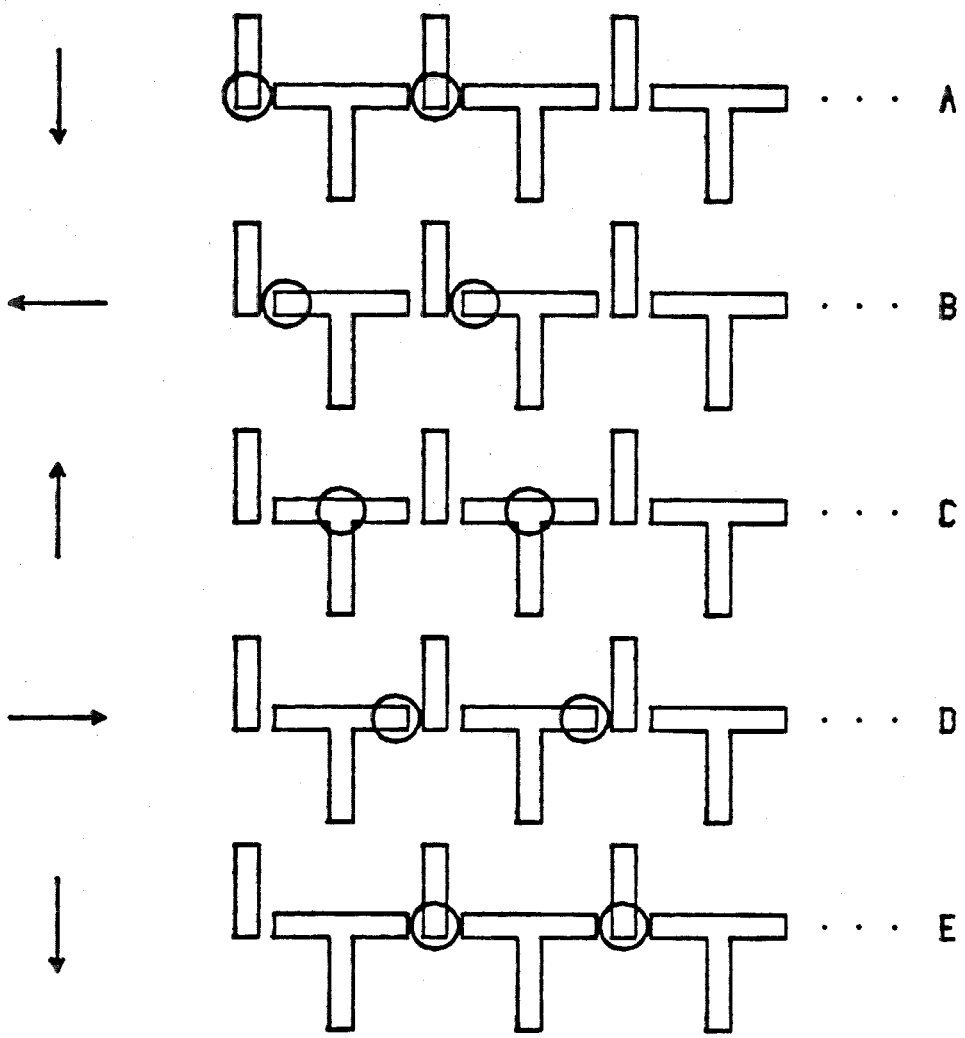

Fig. 1.2. T and I bar bubble propagation structure. The arrows on the left show the direction of the rotating in-plane field. As the in-plane field rotates clockwise the bubble under the permalloy overlay propagates in the +x direction. A single T and I bar pair constitutes a cell of the shift register.

closer to the bubble so that it moves there. When the in-plane field rotates to the x direction (Case D) the bubble moves to the right side of the T bar. When the in-plane field rotates to the -y direction (Case E) the bubble moves to the bottom of the next I bar. Hence the bubble moves a single period each time the in-plane field rotates by 2π. A shift register is obtained with each T and I bar combination forming a cell able to hold one bit of information.

The function of information storage can be done in digital memory devices using magnetic bubbles [8-11]. One and zero can be represented by the presence or absence of a bubble at a given bit location defined by the permalloy overlay pattern. Permanent magnets are used to provide the bias field necessary for keeping the bubbles stable. The information is stored in this shift register style memory in many parallel closed loops called minor loops. Data will circulate in these loops in the presence of a rotating in-plane field. Access to data is done by transferring [12] the bubbles to a common shift register called the major loop.

The major loop which links all minor loops contains the read [13,14] and write [15] circuits. Writing in bubble memory devices is done by locally decreasing the bias field.

Current pulses through a hairpin shaped conductor overlay nucleate the bubbles. These are then shifted through the major loop and transferred to the minor loops for storage. Reading is done by transferring the data in the minor loops to the major loop and shifting the data to the read circuit. Here the detection of bubble is done by utilizing the magnetoresistive effect [15]. The bubble is stretched and passed underneath permalloy material which changes its resistance due to the stray fields from the bubble.

A complete bubble memory package [17,18] can be built by housing the bubble chip between coils and permanent magnets. The magnetic overlays for the chip are fabricated by photolithographic techniques. Then the bubble chip is located between two orthogonal concentric coils which supply the rotating in-plane field necessary to propagate the bubbles. A pair of permanent magnets is added to the top and bottom of the chip to supply the bias field. This chip-coil-magnet assembly is then housed in magnetically shielded dual in-line packages slightly larger than standard microprocessor packages. Presently bubble memory packages with up to 1 Mbit capacity and 10^5 bits/sec data rate are commercially available [18].

Bubble devices have significant advantages in the information storage technology. Bubble materials are easy

to grow [19] and require low temperature processing. They require only one to two levels of high resolution lithography due to simple device structure and high yields are obtained. The stored data is non-volatile, that is, the information is retained even when a power failure occurs, since bubbles are kept stable using permanent magnets. Other advantages of being non-mechanical are that the physical size of bubble devices are small and they use little power. Also bubble devices are simple to interface with other devices. In the memory hierarchy, in terms of access time and cost per bit, the bubble device fills the gap between semiconductor memory and magnetic disk.

1.3 Bubble Materials

For a magnetic material to support bubbles, the anisotropy must be directed normal to the plane and must be high enough, compared to the magnetization, so that the sample will remain magnetized in that direction [20,21]. The quality factor, Q, is usually used to characterize the material. It is defined as the ratio of the anisotropy field (H_k) to the magnetization ($4\pi M_s$):

$$Q = \frac{H_k}{4\pi M_s} \qquad (1.1)$$

The demagnetizing field energy, proportional to $4\pi M_s$, is

lowest if the magnetization is in the plane of the sample. On the other hand the anisotropy energy, proportional to H_k, is lowest if the magnetization is normal to the sample. When the anisotropy field is larger than the demagnetizing field, i.e., the condition $Q > 1$, the magnetization will remain magnetized normal to the plane and only then stable cylindrically shaped domains are possible. This condition on Q distinguishes bubble films from all other practical magnetic materials except the hardest permanent magnets. It has been shown that the bubble stability range is reduced if Q is too near this limit. Also unwanted nucleation of bubbles can occur in devices if Q is too low [22]. To have reasonable device operation Q should be larger than 3 [9,23]. On the other hand if Q is too high it is difficult to nucleate bubbles in devices. A typical range for Q in bubble devices is $3 \leq Q \leq 8$.

The bubble material requirements in devices are determined by the restrictions on the static stability range and the velocity of the bubble. In bubble devices the packaging of the domains is limited to a spacing of four bubble diameters due to the magnetostatic interaction between them. To achieve lower costs it is desirable to make the bubbles as small as possible. On the other hand the lower limit on the bit size is limited by the resolution of the photolithographic technique used to form the magnetic overlays.

Therefore the material is selected with a bubble stability range matching the requirements of the overlay. To discuss bubble stability it is convenient to define the material parameter intrinsic length [2,3] as

$$\ell = \frac{\sqrt{AK}}{\pi M_s^2} \qquad (1.2)$$

where A is the exchange energy constant and K is the anisotropy energy constant. The stability conditions are found by energy minimization using variational techniques. At a thickness equal to 4ℓ, it is found that the domain diameter and its dependence on thickness is minimized and the ability of the domain to recover from fluctuations in size and shape in the presence of coercivity is maximized [2]. At this thickness the ratio of the bias field at collapse to the bias field at stripeout is 1.4 and the ratio of the stripeout diameter to collapse diameter is 3. The domain diameter is equal to 8ℓ at the center of this stable region. The thickness of 4ℓ and the domain diameter of 8ℓ are called preferred values in bubble materials. Another requirement for bubble materials is that the velocity of the bubble should be high for high data rates in devices. Solution of the equations of motion [24] show that the velocity of a bubble is proportional to the mobility

$$\mu = \frac{\gamma}{\alpha}\sqrt{\frac{A}{K}} \qquad (1.3)$$

where γ is the gyromagnetic ratio and α is the damping parameter. Hence low damping materials with high gyromagnetic ratios are preferred. Also low coercivity is required for high velocity and small defect density for uniform motion.

Orthoferrites [1,4], hexaferrites [25], amorphous [20,26,27] materials and rare-earth garnets [21,28,29] have composition ranges where $Q > 1$, hence, bubble domains are possible. Orthoferrites support bubbles and have high velocities but the bubble diameters are so large ($d > 20$ microns) that practical storage densities cannot be achieved. Also the material must be cut from bulk single crystal materials that are hard to grow so that large wafers for low cost are not practical. In hexaferrites small bubble diameters ($d \sim 8$ microns) can be obtained but the maximum obtainable bubble velocity is too low for device data rates. Also a non-uniform coercive force affects the bubble propagation. Amorphous bubble materials can support small bubbles ($d \leq 2$ microns) and have high velocities. They have low cost and the existing semiconductor technology can be used in their manufacture. Unfortunately the material

parameters, especially coercivity, are highly temperature sensitive and other bubble parameters are hard to control. Rare-earth garnets have suitable properties to be used in high performance devices. Garnets can support small bubbles ($d \leq 4$ microns) compatible with the present state of art photolithography. High velocities for high data rates are also possible. The material can be grown from the liquid phase allowing the bubble parameters to be easily tailored for specific purposes. The large single crystal garnet films have a low coercivity as well as low defect density.

Rare-earth garnet materials are presently used as standard bubble materials. They satisfy both the stability and device performance requirements. They are grown as single crystal films having the general formula (rare-earth elements)$_3Fe_5O_{12}$ with typical rare-earth elements used being Eu, Tm, Gd, Sm, Lu, Yb. The magnetic films are grown epitaxially on non-magnetic bulk garnet crystals having the composition $Gd_3Ga_5O_{12}$ [19]. The parameters of garnet materials can be controlled easily by changing the composition of the garnet. The magnitude of $4\pi M_s$ can be adjusted by substituting non-magnetic Al, Ga or Ge ions. The required uniaxial anisotropy is obtained during the growth process and dominates over the cubic crystalline anisotropy. Although its origin

is not understood well it can be controlled easily. Unless considerable improvements are made in other materials, garnets will continue to be the only materials used in devices.

1.4 Bubble Domain Observation Techniques

The magnetooptical Faraday effect [30-33] is particularly useful for observing bubble domains. This effect is the rotation of the plane of polarization of linearly polarized light when it is transmitted through a magnetic medium. Its origin is due to the gyrotropic properties of the medium. Classically the effect is explained by separating the incident linearly polarized light wave into right and left circularly polarized waves. Each has a different effective index of refraction through the magnetic medium, i.e., there is circular birefringence and the two waves travel with different velocities. When the two circularly polarized waves are recombined after passing through a magnetic medium, again linearly polarized light is obtained but with its axis rotated by a small amount. This rotation is called the Faraday effect. The magnitude of rotation is proportional to the magnitude of magnetization of the sample along the propagation direction and the propagation path length.

A polarizing microscope is most convenient for observing bubble domains [34]. Garnet materials are transparent to green light. The Faraday rotation is generally very small (less than 2×10^3 degree/cm) but the figure of merit (rotation/absorption) is large enough for domain observations. Light is passed through a polarizer, garnet and analyzer in a direction normal to the plane of the sample. The optical axis of the analyzer is rotated with respect to the polarizer until the domains magnetized in one direction are observed as dark while the domains magnetized in the opposite direction are observed as light. With this arrangement, the bubble domain can be easily seen. Another arrangement is also convenient when the boundary or wall between domains is of primary interest rather than the domain itself. For this case the optical axes of the analyzer and polarizer are perpendicular so that domains magnetized in opposite directions are observed as the same shade of gray. Under this condition the domain wall separating the domains is a dark line due to diffraction in the sample by the domain wall. Using this crossed polarizer mode, precise measurements of the position of the domain wall can be made.

The magnetooptical Kerr effect [32-33, 35] is very similar to the Faraday effect only it occurs when light is

reflected from a magnetic medium. Calculation of reflection coefficients using the boundary conditions at the surfaces of a magnetic medium show that the plane of polarization of the reflected light is rotated with respect to the incident light. This is due to the phase difference between the right and left circularly polarized waves forming the reflected wave. This rotation is called the Kerr effect. Its magnitude depends on the angle of incidence of light and the magnitude and direction of the magnetization at the surface. The reflected light in the Kerr effect is elliptically polarized as a result of the magnitude difference between the right and left circularly polarized waves.

The properties of the Kerr effect require special considerations for domain observations. The material must be opaque at the wavelength of light used for minimum absorption during reflection and a high figure of merit. Blue light has to be used in bubble materials for this purpose. Also the magnitude of the Kerr rotation is too small for domain observation in typical bubble materials and also the ellipticity of the light obscures the contrast. In a special class of materials, bismuth containing garnets [36], the Kerr rotation is high enough (about 0.5^{o}) and reasonable contrast is obtained. Using this type of material the

domains at the surface can be observed by reflecting light at a normal angle from the surface. The polarizer and analyzer axes are adjusted to change the contrast of domains with respect to each other. In the crossed polarizer mode the domain wall is observed as a dark line as in the Faraday effect. This mode in Kerr effect is particularly important to study the characteristics of the wall only near the surfaces whereas in Faraday effect the wall in the bulk of the film is observed. Using both the Faraday and Kerr effects in the cross polarizer mode and comparing them, more complete information is obtained about the characteristics of the domain wall.

REFERENCES

1. A. H. Bobeck, Bell Syst. Tech. J. 46, 1901 (1967).
2. A. A. Thiele, Bell Syst. Tech. J. 48, 3287 (1969).
3. A. A. Thiele, J. Appl. Phys. 41, 1139 (1970).
4. A. H. Bobeck and E. Della Torre, Magnetic Bubbles (North-Holland 1975).
5. A. J. Perneski, IEEE Trans. MAG-5, 557 (1969).
6. B. D.Cullity, Introduction to Magnetic Materials (Addison-Wesley 1972).
7. S. Chikazumi, Physics of Magnetism (John Wiley and Sons 1964).
8. H. Chang, Magnetic Bubble Technology: Integrated Circuit Magnetics for Digital Storage and Processing (IEEE Press, John Wiley, 1975).
9. A. H. Bobeck, P. I. Bonyhard, and J. E. Geusic, IEEE Proc. 63, 1176 (1975).
10. A. H. Bobeck and H. E. D. Scovil, Scientific American 224, 78 (June, 1971).
11. A. B. Smith, Bubble-Domain Memory Devices (Artech House, Dedham, Mass., 1974).
12. P. I. Bonyhard, Y. S. Chen and J. L. Smith, AIP Conf. Proc. 18, 100 (1974).

13. L. R. Tocci, P. K. George, and J. L. Archer, AIP Conf. Proc. 10, 197 (1972).

14. W. Strauss, A. H. Bobeck, and F. J. Ciak, AIP Conf. Proc. 10, 202 (1972).

15. T. J. Nelson, Y. S. Chen, and J. E. Geusic, IEEE Trans. MAG-9, 289 (1973).

16. W. Strauss, Proc. IEEE 58, 1386 (1960).

17. S. Orihara, R. Knoshita, T. Yanesc, M. Segawa, S. Metsuyama, K. Yamagishi, J. Appl. Phys. 49, 1930 (1978).

18. J. L. Archer, Digest of 1977 Intermag. Conf.

19. Georg Hass, Physics of Thin Films (Academic Press 1977).

20. J. W. Nielsen, IEEE Trans. MAG-12, 327 (1976).

21. U. F. Gionole, D. H. Smith, A. A. Thiele and L. G. von Vitert, IEEE Trans. MAG-5, 558 (1969).

22. M. H. Kryder, K. Y. Ahn and J. V. Powers, Digest of 1975 Intermag. Conf.

23. W. J. Bonte, AIP Conf. Proc. 5, 140 (1972).

24. N. L. Schryer and L. R. Walker, J. Appl. Phys. 45, 5406 (1974).

25. L. G. Van Uitert, D. H. Smith, W. A. Bonner, W. H. Grodkiewicz and G. J. Zydzik, Mater. Res. Bull. 5, 455 (1970).

26. C. H. Bajorek, and R. J. Kobliska, IBM J. Res. and Develop. 20, 271 (1976).

27. P. Chaudhari, T. J. Coumo, and R. J. Gambino, IBM J. Res. and Develop. 17, 66 (1973).

28. A. H. Bobeck, et al, Appl. Phys. Lett. 17, 131 (1970).

29. D. M. Heinz, P. J. Besser, J. M. Owens, J. E. Mee, and G. R. Pulliam, J. Appl. Phys. 42, 1243 (1971)

30. R. Carey, and E. D. Isaac, Magnetic Domains and Techniques for Their Observation (Academic Press 1966).

31. H. Lachowicz, Magnetic Bubbles - Proceedings of the Winter School on New Magnetic Materials - 1975 (Poland 1976).

32. M. I. Freiser, IEEE Trans. MAG-4, 152 (1967).

33. J. L. Suits, IEEE Trans. MAG-8, 95 (1972).

34. F. B. Humphrey, IEEE Trans. MAG-11, 1679 (1979).

35. D. Treves, J. Appl. Phys. 32, 358 (1961).

36. S. Wittekoek, T. J. A. Popme, J. M. Robertson, AIP Conf. Proc. 18, 944 (1974).

CHAPTER 2

Domain Walls and Domain Wall Dynamics

The velocity of a domain wall in magnetic bubble garnet material is important for device operation. The device operating frequency in a bubble memory depends on the propagation rate of the bubble which in turn is a function of the domain wall velocity. In bubble films there are limitations on the velocity arising from changes in the internal structure of the wall. To achieve high performance levels required for practical application, it is desirable to understand the physics of these limitations. The velocity of the wall under different field conditions is of particular interest. Here the domain wall velocity dependence on a wide range of drive and in-plane fields has been studied.

The coordinate system most convenient for discussing bubble domain wall physics is the spherical coordinate system as shown in Fig. (2.1). Here the z axis is normal to the sample plane. The magnetization, M_s, makes an angle of θ with this axis. The projection of M_s onto the xy plane makes an angle of ϕ with the x axis. The polar coordinates θ and ϕ are functi ns of the cartesian

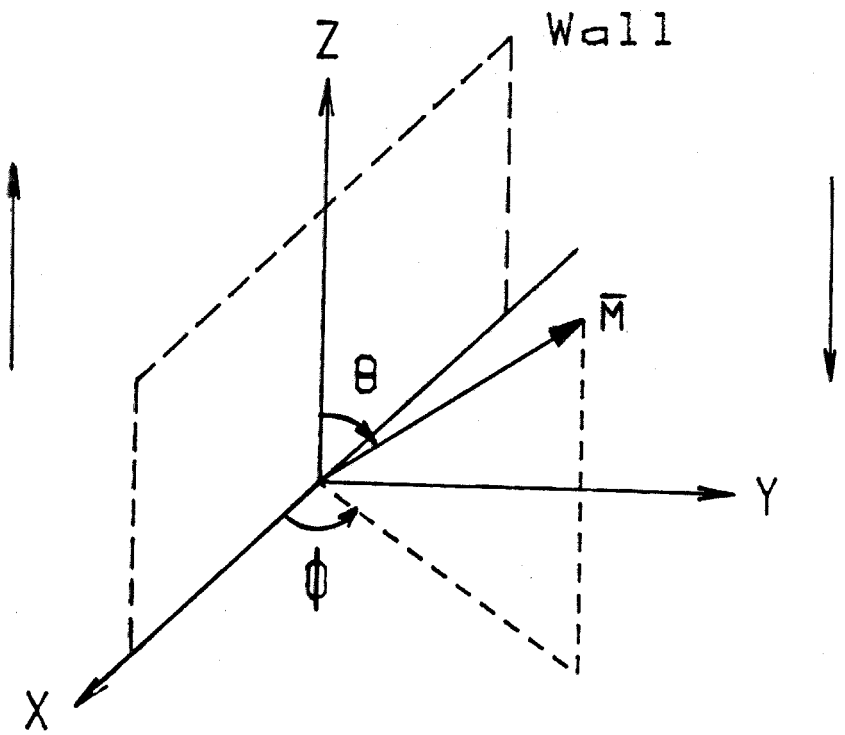

Figure 2.1. The spherical-coordinate system used to describe the orientation of $\bar{M}$. The z axis is normal to the plane of the sample. The domain wall lies in the xz plane.

coordinates x, y and z. When domain walls are considered, it is convenient for them to be in the xz plane as shown in the figure. Their motion is in the y direction.

2.1 Static Domain Wall Structure

Magnetostatics

The total static energy density in a magnetic material is composed of terms representing anisotropy, exchange, demagnetizing fields and externally applied fields. It is given by

$$E_T = E_K + E_A + E_D + E_H \qquad (2.1)$$

Here the one-dimensional forms of the energy terms will be discussed where the polar coordinates θ and ϕ are allowed to change only in the y direction. In garnet materials there is an easy axis of uniaxial anisotropy normal to the sample plane. The lowest anisotropy energy state is when the magnetic moments are aligned parallel to this axis. The uniaxial anisotropy energy per unit volume, E_k, due to the magnetic moments making an angle of θ with the easy axis along the z coordinate is given by

$$E_K = K \sin^2\theta \qquad (2.2)$$

where K is the anisotropy energy constant in ergs/cm^3. The exchange energy is due to neighboring magnetic moments not being parallel to each other and is proportional to the spatial rate of change of the angle between nearest neighbor moments. The lowest exchange energy state is when all the magnetic moments are parallel. The exchange energy is given in one dimension by

$$E_A = A\left(\frac{d\theta}{dy}\right)^2 + A \sin^2\theta\left(\frac{d\phi}{dy}\right)^2 \qquad (2.3)$$

where A is the exchange energy constant in erg/cm. The source of the demagnetizing field energy is the divergence of magnetization. This energy is the most difficult to deal with since it is usually very complicated and most of the time it must be approximated rather than calculated. In one dimension, however, it is rather simple

$$E_D = 2\pi M_s^2 \sin^2\theta \sin^2\phi \qquad (2.4)$$

The external field or Zeeman energy is the potential energy of the magnetization with an applied field

$$E_H = -\bar{M} \cdot \bar{H}_E \qquad (2.5)$$

where H_E is the combination of all externally applied fields. Hence the total energy density, E_T, is given in one dimension by

$$E_T = K \sin^2\theta + A\left(\frac{d\theta}{dy}\right)^2 + A \sin^2\theta\left(\frac{d\phi}{dy}\right)^2 + 2\pi M_s^2 \sin^2\theta \sin^2\phi - \bar{M} \cdot \bar{H}_E \qquad (2.6)$$

Wall Structure in Infinite Sample

A domain wall is the narrow region between two domains where the magnetization rotates rapidly with respect to the domain dimensions from the direction in one domain to the direction in the other. Conceptually the wall separates two semi-infinite spaces, the one with the magnetization pointing along the +z direction ($y < 0$) and the one with the magnetization pointing along the -z direction ($y > 0$). The wall is centered at $y = 0$ and extends in the xz plane as in Fig. (2.1)

The static wall shape can be found by equating the torque on the magnetic moments to zero and solving the resulting coupled partial differential equations with the specific boundary conditions [1]. The boundary conditions

are such that $\theta = 0$ at $y = -\infty$ and $\theta = \pi$ at $y = +\infty$. The torque is obtained from the variational derivatives [2] of the total energy expression Eq. (2.6). Taking the variational derivatives

$$\frac{\delta E_T}{\delta \theta} = \frac{\partial E_T}{\partial \theta} - \frac{\partial}{\partial y}\left[\frac{\partial E_T}{\partial (\frac{\partial \theta}{\partial y})}\right] \tag{2.7a}$$

$$\frac{\delta E_T}{\delta \phi} = \frac{\partial E_T}{\partial \phi} - \frac{\partial}{\partial y}\left[\frac{\partial E_T}{\partial (\frac{\partial \phi}{\partial y})}\right] \tag{2.7b}$$

we get

$$K \sin 2\theta - 2A \frac{d^2\theta}{dy^2} + A \sin 2\theta \left(\frac{d\phi}{dy}\right)^2 + 2\pi M_s^2 \sin 2\theta \sin^2\phi = 0 \tag{2.8a}$$

$$-2A \sin 2\theta \frac{d\theta}{dy}\frac{d\phi}{dy} + 2\pi M_s^2 \sin^2\theta \sin 2\phi - 2A \sin^2\theta \frac{d^2\phi}{dy^2} = 0 \tag{2.8b}$$

The specific solutions of interest here are

$$\phi(y) = 0 \quad \text{or} \quad \phi(y) = \pi \tag{2.9}$$

and

$$\theta(y) = 2 \arctan\left[\exp\left(\frac{y}{\Delta}\right)\right] \qquad (2.10)$$

where $\Delta = \sqrt{\frac{A}{K}}$ is called the wall width parameter. The assumptions leading to the wall shape, Eq. (2.10), are called Bloch wall assumptions [3]. The most important consequence is that there is no demagnetizing term in the total energy of a Bloch wall since the azimuthal angle is assumed constant across the wall (Eq. (2.9)) and there is no divergence of magnetization. Hence in an infinite material the shape of the one-dimensional wall is determined only by anisotropy and exchange. The exchange energy is minimum when the magnetic moments are parallel to each other, and it favors a gradual change in the direction of the magnetization. The anisotropy energy is minimum when the magnetization is all along the anisotropy axis and it favors an abrupt change in the direction of the magnetization. The balance between the exchange energy and the anisotropy energy determines the spatial rate of rotation of the magnetization from one domain to the other and hence its width.

The one-dimensional wall shape in an infinite material, Bloch wall, is shown in Fig. (2.2). Here the polar angle

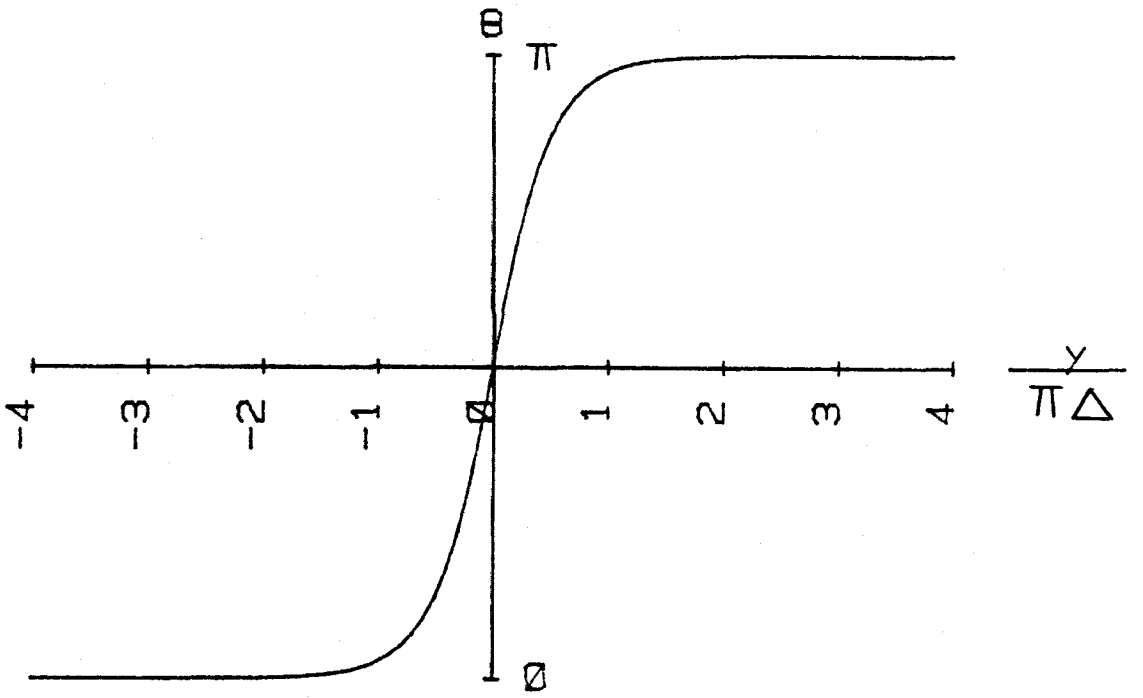

Figure 2.2. The polar angle shown as a function of distance perpendicular to the wall in units of wall width for a Bloch wall. Most of the rotation is concentration in a region of width $\pi\Delta$ around the center.

is shown as a function of the distance perpendicular to the wall in units of $\pi\Delta$. As seen the change in $\theta(y)$ from 0 to π occurs mainly in a region $\pi\Delta$ wide. This width is called the domain wall width. In bubble materials the Bloch wall width, $\pi\Delta$, is typically 0.1 micron . The two solutions $\phi = 0$ and $\phi = \pi$ are for clockwise and counterclockwise rotation of the magnetic moments, respectively, going through the wall in the +y direction while the shape is the same as in Fig. (2.2). This sense of rotation is called the chirality of a bubble.

The Bloch wall energy per unit area is obtained by integrating the total energy per unit volume [4]. The result is

$$\sigma_o = \int_{-\infty}^{\infty} E_T \, dy = 4\sqrt{AK} \qquad (2.11)$$

where σ_o is the wall energy/area and E_T is the total energy expression from Eq. (2.6). Here the external fields are taken to be zero. As seen there is no magnetization term in the expression since the demagnetizing energy is zero for a Bloch wall.

The domain wall shape along the in-plane field (H_{ix}) in an infinite sample is calculated in the same way as with

no in-plane field applied. The only added term to the total energy is the Zeeman term due to the in-plane field. The possible demagnetizing field energy term is assumed zero as in Bloch wall assumption because there is no divergence of magnetization caused by the field and the magnetic moments are in the plane of the wall. Without this term it is possible to find an analytic expression for the wall shape. The energy density per unit volume is

$$E_T = K \sin^2\theta - K \sin^2\theta_o + A\left(\frac{d\theta}{dy}\right)^2 \qquad (2.12)$$

$$- H_{ix} M_s \sin\theta + H_{ix} M_s \sin\theta_o$$

where $\theta_o = \arcsin(H_{ix}/H_K)$. The energy terms containing θ_o are the constant energy independent of the wall and satisfy the boundary conditions far from the wall. Taking the variational derivative of the total energy to find the torque and equating it to zero gives

$$K \sin 2\theta - H_{ix} M_s \cos\theta - 2A \frac{d^2\theta}{dy^2} = 0 \qquad (2.13)$$

The solution for the boundary conditions $\theta = \pi/2$ at $y = 0$ and $d\theta/dy = 0$ at $\sin\theta = H_{ix}/H_K$ is

$$y = \sqrt{\frac{A}{K}} \frac{1}{\sqrt{1 - x^2}} \quad . \tag{2.14}$$

$$\ell n \left| \frac{(1-x+\sqrt{1-x^2})\tan\frac{\theta}{2} + (1-x) - \sqrt{1-x^2}}{(1-x-\sqrt{1-x^2})\tan\frac{\theta}{2} + (1-x) + \sqrt{1-x^2}} \right|$$

where $x = H_{ix}/H_K$. This solution is with the H_{ix} parallel to the wall in the direction of the magnetization in the middle of the wall. For H_{ix} opposite to the magnetization in the middle of the wall -x has to be substituted for x in Eq. (2.14). Note that the solution is the Bloch wall solution for $H_{ix} = 0$.

The wall shape, $\theta(y)$, with an in-plane field applied parallel to the wall in the direction of the magnetization in the middle of the wall can be seen in Fig. (2.3). Here the polar angle $\theta(y)$ is shown as a function of distance normal to the wall in units of Bloch wall width, $\pi\Delta$. The wall shape without an in-plane field, Eq. (2.10), is also shown in dashed lines for comparison. The magnitude of the normalized in-plane field is chosen to be $H_{ix}/H_K = 0.1$. In the materials of interest here the applied fields are

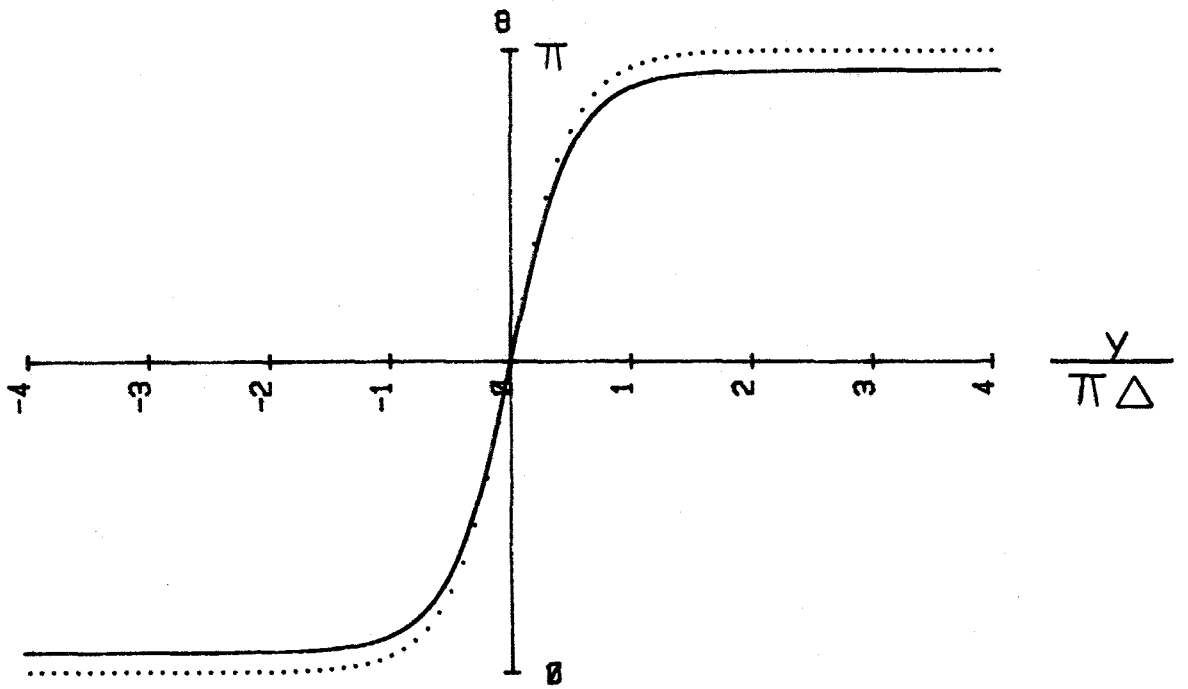

Figure 2.3. The polar angle shown as a function of distance perpendicular to the wall for an in-plane applied along the wall. The in-plane field magnitude is 10% of the anisotropy. The dotted line is Bloch wall shape with no in-plane field.

typically less than 10% of the anisotropy. It can be seen that neither the domain wall shape nor width has appreciably changed. For all practical purposes the wall shape, Eq. (2.10), without an in-plane field can be used instead of Eq. (2.14).

For the domain wall in an infinite sample normal to an in-plane field (H_{iy}) the wall shape is difficult to calculate due to the demagnetizing field energy, however, approximations can be made. Here the demagnetizing field energy is not zero since the magnetization is not in the plane of the wall. It is energetically more favorable for the magnetization to rotate out of the wall plane in the presence of an in-plane field normal to the wall and divergence of magnetization is present. This causes the total energy expression, Eq. (2.6) to be complicated and analytical solutions from the resulting torque equations are hard to obtain. On the other hand to the first approximation the wall shape $\theta(y)$ can be set equal to the Bloch wall shape. This way $\phi(y)$, assumed to be constant across the wall, is determined by a balance between the in-plane field and demagnetizing field. Taking the variation of the total energy and equating the resulting torque equations to zero gives

$$\phi(y) = \arcsin\left(\frac{H_y}{8M}\right) \qquad H_y \leq 8M \qquad (2.15a)$$

$$\phi(y) = \frac{\pi}{2} \qquad H_y \geq 8M \qquad (2.15b)$$

An analytical expression for the wall shape $\theta(y)$ is possible when $\phi(y) = \pi/2$ [5]. Here the resulting torque equations reduce to ones similar for the case of wall along the in-plane field but with $K \rightarrow K+2\pi M_s^2$. The form of the solution is the same as Eq. (2.14) but with $K \rightarrow 2\pi M_s^2$ and the shape of the wall is similar to Fig. (2.3) for $H_{iy}/H_K = 0.1$. For materials considered here $K >> 2\pi M_s^2$ and the approximation that the wall shape is the same as Bloch wall is good as long as the applied fields are low compared to the anisotropy.

Wall Structure in Bubble Thin Film

Bubble materials are thin films so that the assumption of an infinite sample is not appropriate. The magnetization at the sample surfaces is discontinuous and fields are present on the domain wall due to the divergence of magnetization there. The components of these fields in the plane of the sample are called stray in-plane fields. They are non-

uniform through the thickness and affect the internal wall structure. In the materials considered here the domain wall width is much smaller than the film thickness and domain size, and hence the stray fields do not depend on the wall structure. Calculations for different configurations of domains are made by assuming that the wall width is zero and that the magnetization is along the anisotropy axis at all places. These assumptions are good when $Q>>1$. The stray in-plane fields are in a direction normal to the wall plane.

The stray in-plane field profile through the thickness in bubble thin films can be calculated by integrating the divergence of magnetization over the magnetic domains. The wall width is assumed to be zero in all cases. The stray in-plane field is given by

$$H_s(\bar{r}) = -\frac{\partial}{\partial y} \iiint \frac{\bar{\nabla}' \cdot \bar{M}(\bar{r}')}{|\bar{r}-\bar{r}'|} d^3\bar{r}' \qquad (2.16)$$

where the field is in the y direction. The simplest case to calculate is for an isolated wall separating two semi-infinite domains in a sample of thickness h. The result is[7]

$$\frac{H_s(z)}{4\pi M_s} = \frac{1}{\pi} \ell n \left[\frac{z}{h - z} \right] \qquad (2.17)$$

For a stripe array with a spacing of d between the walls the result is [8]

$$\frac{H_s(z)}{4\pi M_s} = \frac{1}{\pi} \ln \left[\frac{\tanh\left[\frac{\pi h}{2d}(z)\right]}{\tanh\left[\frac{\pi h}{2d}(h-z)\right]} \right] \qquad (2.18)$$

For a bubble with a radius of r_o the result is [9]

$$\frac{H_s(z)}{4\pi M_s} = \frac{1}{\pi} \int_0^{\pi/2} \int_0^{2r_o \sin\theta} \rho^2 \left\{ \frac{1}{(\rho^2 + z^2)^{3/2}} + \frac{1}{(\rho^2 + (h-z)^2)^{3/2}} \right\} \sin\theta \, d\rho \, d\theta \qquad (2.19)$$

Note that all the fields diverge logarithmically at the surfaces which is physically unrealistic. This is as a result of taking the wall width zero and having the divergence of magnetization at the surface change abruptly. The actual field will be finite due to the domain wall having a finite width and the surface divergence of magnetization changing smoothly. On the other hand the fields within a few wall widths of the surfaces do not affect any results appreciably. The finite fields resulting from this smooth

variation can be simulated by the transformation [8]

$$z \rightarrow z - \frac{2\Delta \sinh\left(\frac{z}{2\Delta}\right)}{\cosh\left(\frac{h}{4\Delta}\right)} \qquad (2.20)$$

This transformation eliminates the singularities at the surfaces and does not change the profile through the thickness except within a few wall widths from the surfaces.

The stray in-plane field profiles for different configurations of domains are shown in Fig. (2.4). The magnitude of the stray field in the y direction in units of the magnetization is shown as a function of distance through the thickness in units of thickness. The transformation (2.20) is used along with the formulas. Curve (a) is for an isolated wall (Eq. 2.17), Curve (b) is for a stripe array (Eq. 2.18) and Curve (c) is for a bubble domain (Eq. 2.19). The period of the stripe array is taken to be $d = 2.2h$ and the radius of the bubble $r_o = h/2$, typical in the materials considered here. As seen the results are non-uniform through the thickness and are anti-symmetric with respect to the middle of the thickness. As the width of the stripe array or the size of the bubble gets larger the results approach the isolated wall profile. It is important that the magnitude of the stray fields are

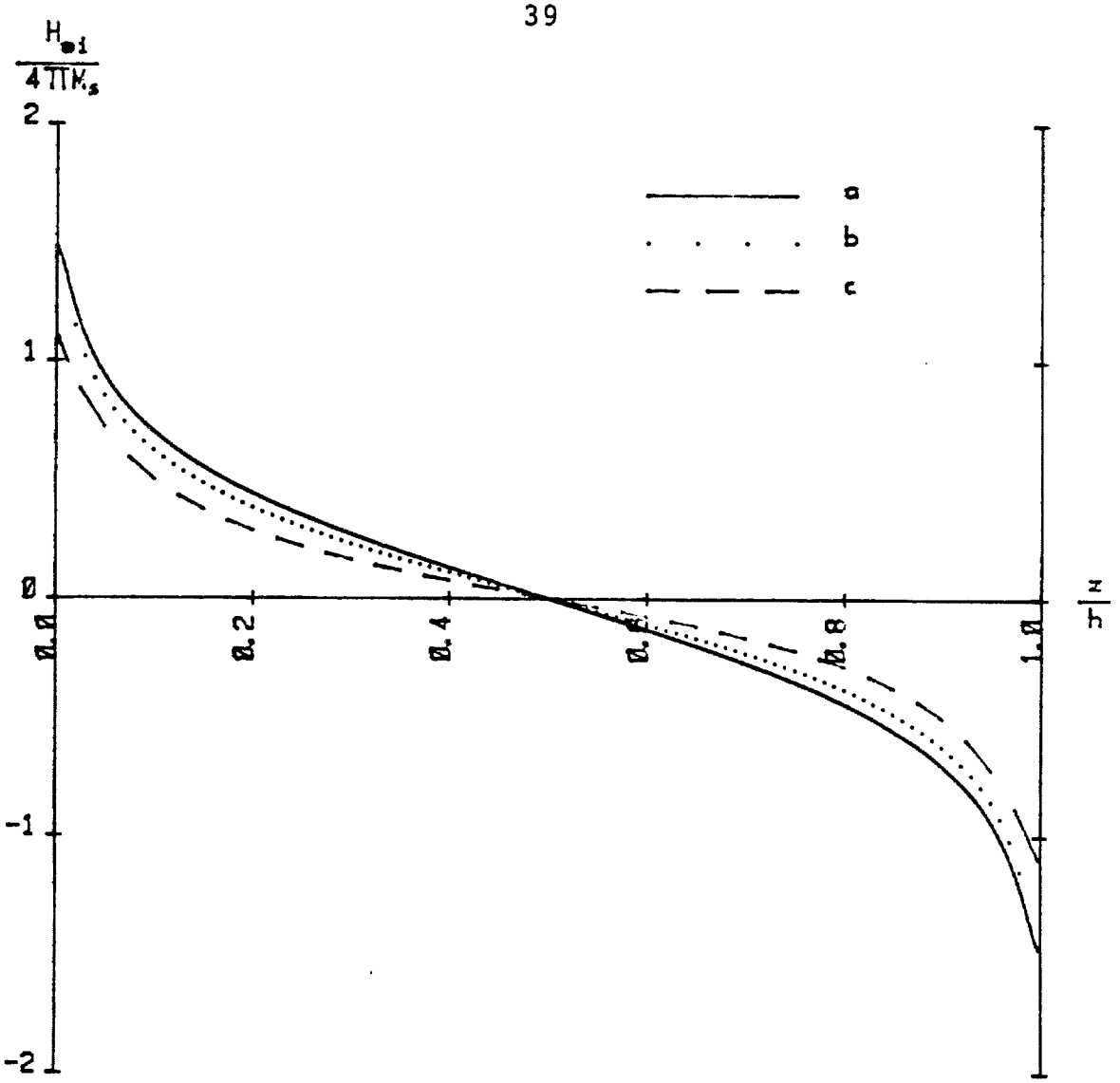

Figure 2.4. The stray in-plane field on the wall in units of $4\pi M_s$ as a function of distance normal to the sample in units of h for (a) isolated wall (b) stripe array with period d = 2.2h and (c) isolated bubble domain with r_o=h/2.

small compared to the anisotropy of the samples studied here and hence the wall shape $\theta(y)$ will not be affected much through the thickness.

In bubble thin films the wall shape $\phi(y)$ changes through the thickness as a result of the stray fields and a twisted wall structure is present. Here $\theta(y)$ will be assumed to be the same through the thickness. The magnitude of the twist angle is a function of the stray fields and can be calculated from Eq. (2.15). For $|H_s| \leq 8M_s$ it is given by

$$\phi(z) = \arcsin\left(\frac{H_s(z)}{8M_s}\right) \tag{2.21}$$

where $H_s(z)$ is the stray field for a bubble domain given by Eq. (2.19). For $|H_s| \geq 8M_s$, $\phi(z)$ is equal to $\pi/2$ or $-\pi/2$ depending on the direction of the stray field.

The twisted wall structure through the thickness in bubble films is shown in Fig. (2.5). Here the azimuthal angle is shown as a function of position normal to the sample plane in units of thickness. As seen, near the surfaces where the stray fields are above $8M_s$, the magnetization is normal to the wall plane, in opposite directions for the upper and lower surfaces. The sharp transition points from $\phi(z) = \pi/2$ and $\phi(z) = -\pi/2$ to Eq. (2.21) are called critical points. In the middle of the thickness,

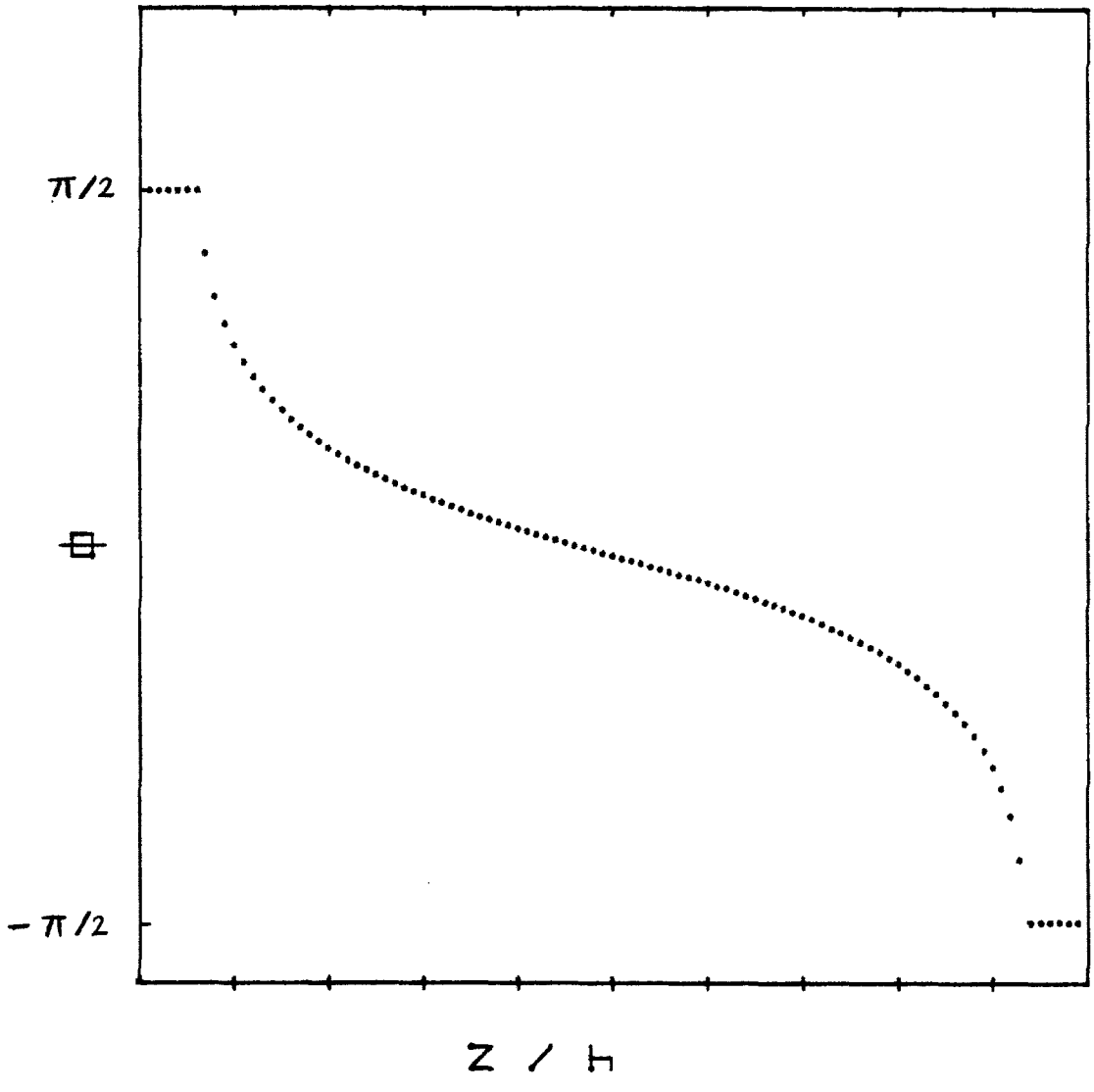

Figure 2.5. Azimuthal angle $\phi(z)$ as a function of position through thickness z/h. The bubble domain stray field, Eq. (2.19) is used in this calculation.

$z = h/2$, there is no stray field and Bloch wall is present. In these calculations the exchange energy due to the twist is neglected. It does not have appreciable effect other than near the critical points where it smooths the variation of the twist.

2.2 Dynamic Domain Wall Structure

Domain wall dynamics is based on the fundamental equation describing the gyroscopic precession of magnetization proposed by Landau and Lifshitz [10]. Here the magnetization per unit volume in the material, M_s, is assumed to be constant in magnitude and continuous as a function of position [11]. Only its direction is allowed to change. The ratio of the angular momentum due to the electron spin to the magnetic moment is given by a constant of proportionality, $-\gamma$, called the gyromagnetic ratio and the torque is given by $\overline{T} = -\dot{\overline{M}}/\gamma$ where the derivative is with respect to time. The gyromagnetic ratio is approximately 1.7×10^7 Oe^{-1} sec^{-1} in the materials used here. The torque on the magnetization can be written in terms of a total effective field and $\overline{T} = \overline{M} \times \overline{H}_{et}$, where $\overline{H}_{et} = \overline{H}_e + \overline{H}_d$. $\overline{H}_e$ can be derived from the differentiation of the total static energy. It includes anisotropy, exchange, external fields, etc. The second term

is phenomenological and represents dissipative effects which cannot be derived from a stored energy. It is given in the Gilbert form by $\bar{H}_d = -\alpha\dot{\bar{M}}/\gamma|M|$ [12], where α is the Gilbert damping parameter typically small compared to one in bubble materials. Combining the equations above, the Landau-Lifshitz equation with Gilbert damping is obtained as

$$\dot{\bar{M}} = -\gamma\bar{M} \times \bar{H}_e + \frac{\alpha}{M_s}\dot{\bar{M}} \times \bar{M} \qquad (2.22)$$

where the first term on the righthand side is the conservative torque (the stored energy does not change) and the second term is the dissipative torque (the stored energy decreases). A precessing moment loses energy due to the dissipative torque and approaches its equilibrium in the direction of the field. When the damping is zero the moment precesses around a uniform field. In a symmetrical situation, this is called Larmor precession and the angular frequency is found from the L.L. equation as

$$\omega = \gamma H_e \qquad (2.23)$$

The wall structure and position with respect to time

under a drive field is studied in two regions. An exact solution [13-15] using the L.L. equation can be found in one dimension for an infinite sample if the drive field is less than a certain critical field. This region is called the linear region where the velocity of the wall is linearly proportional to the drive field. The linear region is well understood and it gives good results in bubble thin films. For drive fields above the critical field the velocity characteristics are not well understood in bubble films. The equations of motion are difficult to solve and approximations have to be made. This region is called the non-linear region where the velocity with respect to the drive field is non-linear. This region will be investigated experimentally in detail in this chapter.

Linear Region

The wall structure and position as a function of time will be calculated when a uniform magnetic field is applied along the anisotropy axis. The wall is in the xz plane with the drive field along the +z direction. The effective field on the magnetization can be found from the differential of the total energy, Eq. (2.6). This way the L.L. equation

gives two coupled partial differential equations for the polar and azimuthal angles of the wall as a function of distance normal to the wall and time [15]. For high Q samples these equations can be reduced to a simple form [2]. The wall shape $\theta(y,t)$ and the azimuthal angle $\phi(y,t)$ across the wall are assumed to be constant during steady motion. Hence the wall is assumed to be moving as a single entity. This way the equations reduce to

$$\dot{q} = \pi\gamma\Delta[2M_s \sin 2\phi + \tfrac{1}{2}H_{ix} \sin\phi - \tfrac{1}{2}H_{iy} \cos\phi] + \alpha\Delta\dot{\phi} \qquad (2.24)$$

and

$$\dot{\phi} = \gamma H_z - \frac{\alpha\dot{q}}{\Delta} \qquad (2.25)$$

where q is the position of the middle of the wall, H_z is the drive field and H_{ix},H_{iy} the in-plane fields. Note that Eq. (2.25) gives Larmor precession in the case of zero damping. The problem is now reduced to two variables as a function of time. A solution can be obtained by setting $\dot{q}=v$, a constant velocity, and $\dot{\phi}=0$. The result is

$$v = \mu H_z = \frac{\gamma}{\alpha}\sqrt{\frac{A}{K}}\, H_z \qquad (2.26)$$

where μ is the mobility given by Eq. (1.3). As seen the velocity is linearly proportional to the drive field. The constant ϕ can be calculated from Eq. (2.24). These solutions are valid below a critical field called the Walker breakdown field. In the case of zero in-plane field it is given by

$$H_c = 2\pi\alpha M_s = \frac{v_c}{\mu} \qquad (2.27)$$

where v_c is the critical velocity. This field is calculated to be typically a few Oe in bubble materials. Above the Walker breakdown field no wall structure that is constant with respect to time is possible. The effect of an in-plane field is to increase H_c, extending the linear region. On the other hand it does not affect the mobility. The results above agree well with the exact solution in the high Q limit. There is good experimental evidence that at low drive fields, domain walls in bubble thin films move in a one-dimensional manner [1,16].

In one-dimensional wall motion the wall moves forward

as a result of an effective field generated normal to the wall. When a drive field is applied normal to the film, the magnetization in the Bloch wall precesses around it. This way the magnetization rotates out of the wall plane causing divergence of magnetization through the wall width. The resulting effective field, called Becker field, is normal to the wall and it precesses the magnetization around it, aligning it with the drive field and hence moving the wall. Therefore, it is the Becker field that moves the wall rather than the drive field. Since the maximum effective field from the divergence of magnetization is limited to $4\pi M_s$ there is an upper limit to the velocity of the wall and Eq. (2.27) follows. On the other hand the Becker field can be increased by adding an in-plane field on the wall thereby increasing the critical velocity and drive field.

Non-linear Region

In the one-dimensional model for drive fields higher than the Walker breakdown field the velocity decreases non-linearly with drive and then increases again with a small mobility at still higher drives. Calculations using Eq. (2.24) and Eq. (2.25) without in-plane fields show that for $H_z > H_c$ the azimuthal angle precesses around the drive

field and the wall motion is oscillatory. This is due to the periodic nature of torque terms with respect to ϕ. The equilibrium that exists between the damping field and the drive field in the linear region keeping ϕ stationary does not exist above the breakdown. In the case of no damping, the wall moves back and forth about its initial position. It moves forward for $0 < \phi < \pi/2$ and $\pi < \phi < 3\pi/2$ and backwards for $\pi/2 < \phi < \pi$ and $3\pi/2 < \phi < 2\pi$ with the total average displacement being zero. Calculations show that in the presence of damping the average forward displacement is higher than the backward one and the wall moves forward in one period. The average velocity in one period drops sharply from the critical velocity as the drive field is increased. For larger drive fields, $H_z >> H_c$, ϕ precesses essentially with Larmor frequency, $\dot{\phi} = \gamma H_z$, and the periodic torque terms average out. The velocity is only determined by the damping torque and

$$v = \frac{\alpha\gamma\Delta}{(1+\alpha^2)} H_z \qquad (2.28)$$

As seen the velocity is again linearly proportional to the drive field but with a mobility α^2 times smaller than the mobility below breakdown.

The region of decreasing velocity is expected to be unstable. If any part of the wall lags behind, the effective drive field increases on that part due to the surface tension of the wall trying to keep it rigid. The surface tension field is a local field due to the wall energy density and is inversely proportional to the radius of curvature of the wall. It is in a direction to smooth the wall and is along the drive field in this case. The increased drive further decreases the velocity of the lagging part and the wall is unstable.

The effect of an in-plane field in the non-linear region is to increase all the velocities [17]. Calculations using Eq. (2.24) and Eq. (2.25) with in-plane field show that the decreasing velocity region extends to higher drives and the velocity is enhanced. The increase in the velocity is due to the higher effective Becker field available during precession. The magnitude of the linear mobility, $\alpha\gamma\Delta$, is not affected but the drive field where this region starts increases with in-plane field. Calculations show that this region is at higher drive fields than the drive fields considered here in the presence of in-plane fields.

In bubble thin films the stray fields from the surfaces generate dynamic wall structures different from the one-

dimensional model. Here variations not only normal to the wall plane but also through the thickness have to be considered. When the drive field is above a critical field a dynamic structure called Horizontal Bloch Line (HBL) is generated [18]. An HBL is a region of rapid rotation of the azimuthal angle in the z direction. It is a transition region between two opposite chiralities. Its width is 0.4 microns, typically few wall widths in bubble materials. A detailed analysis of the HBL theory is beyond the scope of this work and only its effect on the velocity characteristics will be stated here. HBL generation is due to different precession rates of magnetization through the thickness as a result of stray in-plane fields. The critical field for its nucleation is given by

$$H_{ch} = \frac{24.3\ \sqrt{A}}{h} \qquad (2.29)$$

This is typically a few oersteds in bubble materials. Below the HBL nucleation field the domain wall moves in a one dimensional manner as in the linear region [19]. In typical bubble materials the HBL nucleation field is less than the Walker breakdown field. Once the HBL is generated near one sample surface, it is held together by exchange and moves through the thickness towards the other surface.

Here it annihilates and the chirality of the wall is changed by π compared to the initial chirality. Another HBL is generated near this surface and it moves towards the other surface, annihilating there and changing the chirality once more. The resulting velocity from the continuous generation, transport and annihilation of HBL's is constant as a function of the drive field and is called the saturation velocity. It is given by [18]

$$v_s = \frac{7.1\ \gamma A}{h\sqrt{K}} \qquad (2.30)$$

v_s is on the order of 10 m/sec in bubble materials. There is good experimental support for HBL's when the drive field is typically <10 Oe above the HBL nucleation field. It is not clear if the HBL theory extends to higher drive fields in the presence of in-plane fields.

The non-linear region is investigated experimentally in detail in this chapter. Drive fields with magnitudes well above the Walker breakdown and HBL nucleation fields are used. The effect of a static in-plane field along and normal to the wall is studied independently [20].

2.3 Experimental

An optical sampling microscope [21] was used in the experiments. A detailed description of the setup is given in Appendix B. A 10 nsec exposure pulsed laser light is used to image the domains on a silicon intensified target (SIT) TV camera and the images are recorded on video tape. Each frame on the tape represents a single exposure of a transient phenomenon and the laser trigger is delayed with respect to the start of the event each time. When the frames are displayed consecutively a single event is reconstructed although each frame represents a separate event. Reproducibility of a single event can be shown to be very good by taking multiple frames at the same delay. The data is measured electronically from the TV screen.

The bubble radial expansion method [22] is used to measure the wall velocity. In this method, the bubble is initially in equilibrium with a static bias field. A pulse field in a direction opposing this bias field is applied and the bubble expands towards a new equilibrium size. The pulse field is terminated before this new size is reached and the initial conditions are restored. The bubble radius is measured at different times with respect to the start of the pulse field and is plotted as a function of time.

The slope of the radius as a function of time curves give the wall velocity.

During bubble radial expansion the effective drive field on the wall decreases. Initially with no pulse applied the effective field on the wall is zero. The bias field is in equilibrium with the demagnetizing and wall fields (Appendix A). After the pulse field is applied this equilibrium no longer exists and as the bubble expands the demagnetizing field in the direction of the pulse field decreases. The magnitude of this decrease is calculated by taking the difference between the bias field corresponding to the expanded radius and the applied bias field.

When an in-plane field is applied during radial expansion the bubble may expand elliptically. In this case the minor and major axes are measured independently with respect to time and their velocities obtained separately. The effective drive field is found by approximating the elliptical bubbles as round ones with the effective radius equal to the geometric mean of the major and minor axes.

An as-grown rare-earth garnet sample, 2-16-44, was used in the experiments. Its material characteristics are shown in Appendix C.

2.4 Domain Wall Velocity in Bubble Garnet Materials

Wall with No In-plane Field

The bubble radius as a function of time with no in-plane field applied is shown in Fig. (2.6) for three different pulse fields. The pulse fields used are (a) 60 Oe (b) 85 Oe and (c) 153 Oe and the pulses are 1 microsec long. The delay time between two consecutive data points is 20 nsec up to 600 nsec and 100 nsec thereafter. The data for the pulse fields are shifted with respect to each other to compare them clearly. There are two important observations. The first is that the average slopes of the curves are approximately the same for the three pulse fields. Hence the velocity is independent of the drive field, The saturation velocity is 5.4 m/sec. The second observation is that for an individual pulse field

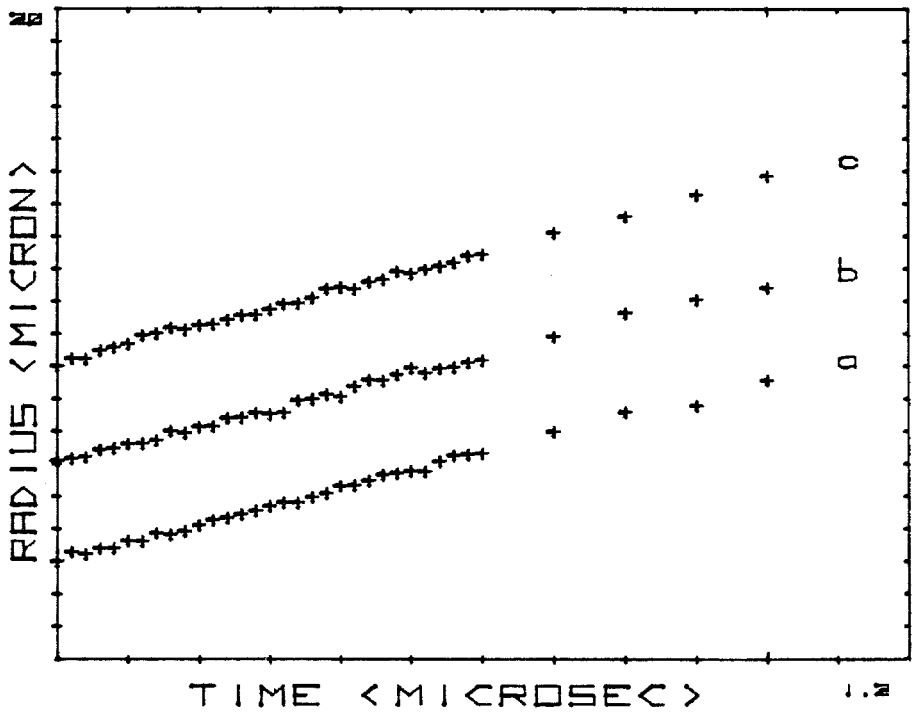

Figure 2.6. The bubble radius measured as a function of time with no in-plane field applied. Three different pulse fields are used: (a) 60 Oe (b) 85 Oe and (c) 153 Oe. The data for the pulses are shifted with respect to each other to compare them clearly.

the curve is fairly straight although the effective drive field on the wall changes as the bubble expands. This field difference at the beginning and end of the pulse field is approximately 31 Oe. This is another indication that the velocity is saturated. Linear curves such as these are characteristic of the data at other high pulse amplitudes.

Wall Along the In-plane Field

The bubble radial distance as a function of time is shown in Fig. (2.7) for three different pulse fields with an in-plane field of H_{ix} = 50 Oe applied along the wall. The pulse fields are 500 nsec long with magnitudes of (a) 60 Oe (b) 99 Oe and (c) 142 Oe. As seen the in-plane field increases the velocity. On the other hand the same observations are made as in the case with no in-plane field. The average velocities are 7.9 m/sec for H_p = 60 Oe, 8.1 m/sec for H_p = 99 Oe and 8.6 m/sec for H_p = 142 Oe and hence do not change appreciably with the drive field. There still exists a saturation velocity as in the case without an in-plane field but with a higher magnitude.

The bubble radial distance as a function of time is shown in Fig. (2.8) for three different pulse fields with an in-plane field of H_{ix} = 300 Oe applied along the wall. The

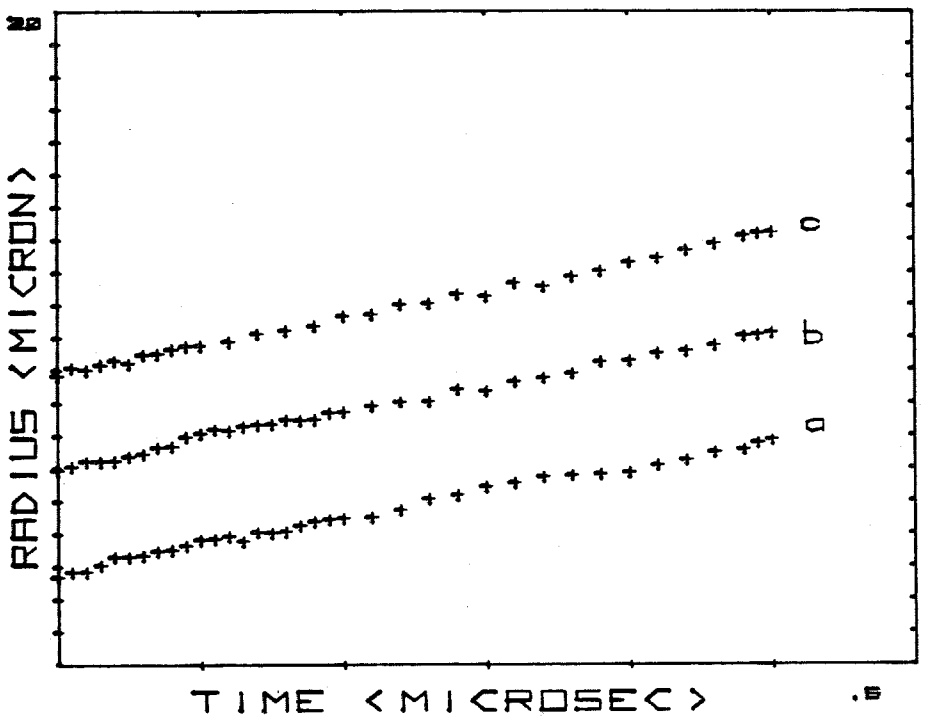

Figure 2.7. The bubble radius measured as a function of time with an in-plane field applied along the wall, H_{ix}=50 Oe. The pulse fields used are (a) 60 Oe (b) 99 Oe (c) 142 Oe.

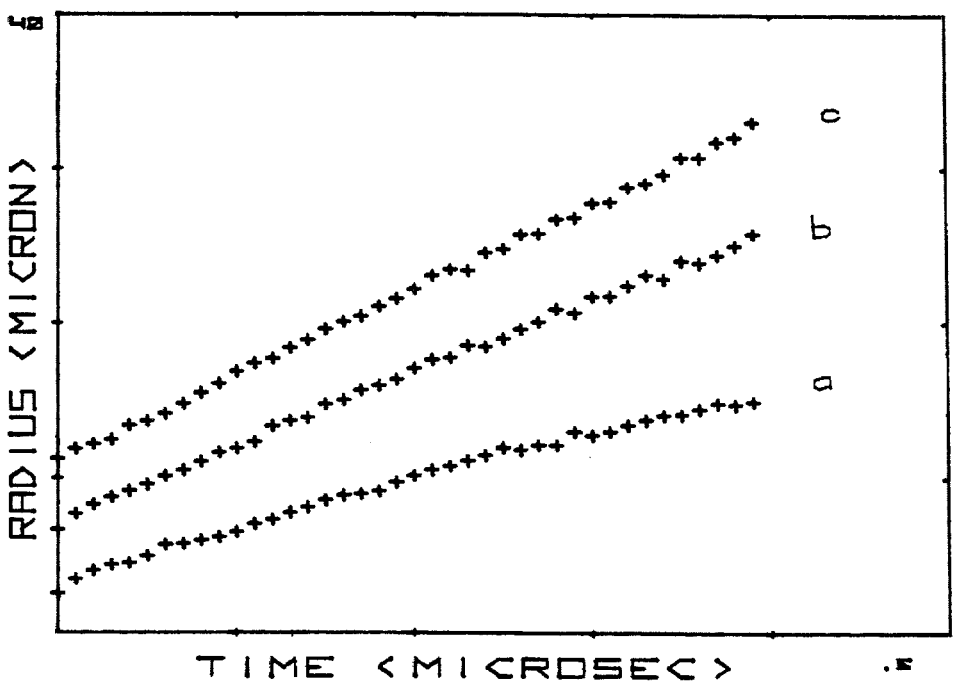

Figure 2.8. The bubble radius measured as a function of time with an in-plane field applied along the wall, H_{ix}=300 Oe. The pulse fields used are (a) 75 Oe (b) 135 Oe (c) 200 Oe.

pulse fields are long with magnitudes of (a) 75 Oe, (b) 135 Oe and (c) 200 Oe. As seen the velocities are further enhanced due to the increase in the in-plane field. For example the velocity is increased from 7.9 m/sec to 35 m/sec when the in-plane field is increased from 50 Oe to 300 Oe. Also the drive field increases the velocity of the wall for the same in-plane field. The velocity increases from 35 m/sec at H_e = 60 Oe to 47 m/sec at H_e = 115 Oe and 55 m/sec at H_e = 175 Oe. The individual curves are not linear as before for the cases of H_p = 75 Oe and H_p = 135 Oe due to the drive field decrease. For the higher drive of H_p = 200 Oe the curve is approximately linear and saturation velocity (v_s = 57 m/sec) is observed.

The average velocity of the wall is shown as a function of the effective drive field with an in-plane field applied along the wall as a parameter in Fig. (2.9). Each point represents the average of data taken from two to five different bubbles. Velocity data is taken in 20 Oe effective field change steps. The in-plane field is varied up to 400 Oe, and the solid lines are drawn by hand to separate the different in-plane field data. A saturation velocity is clearly seen for no in-plane field applied. The general effect of the in-plane field is to increase the saturation velocity. It can be seen that v_s increases

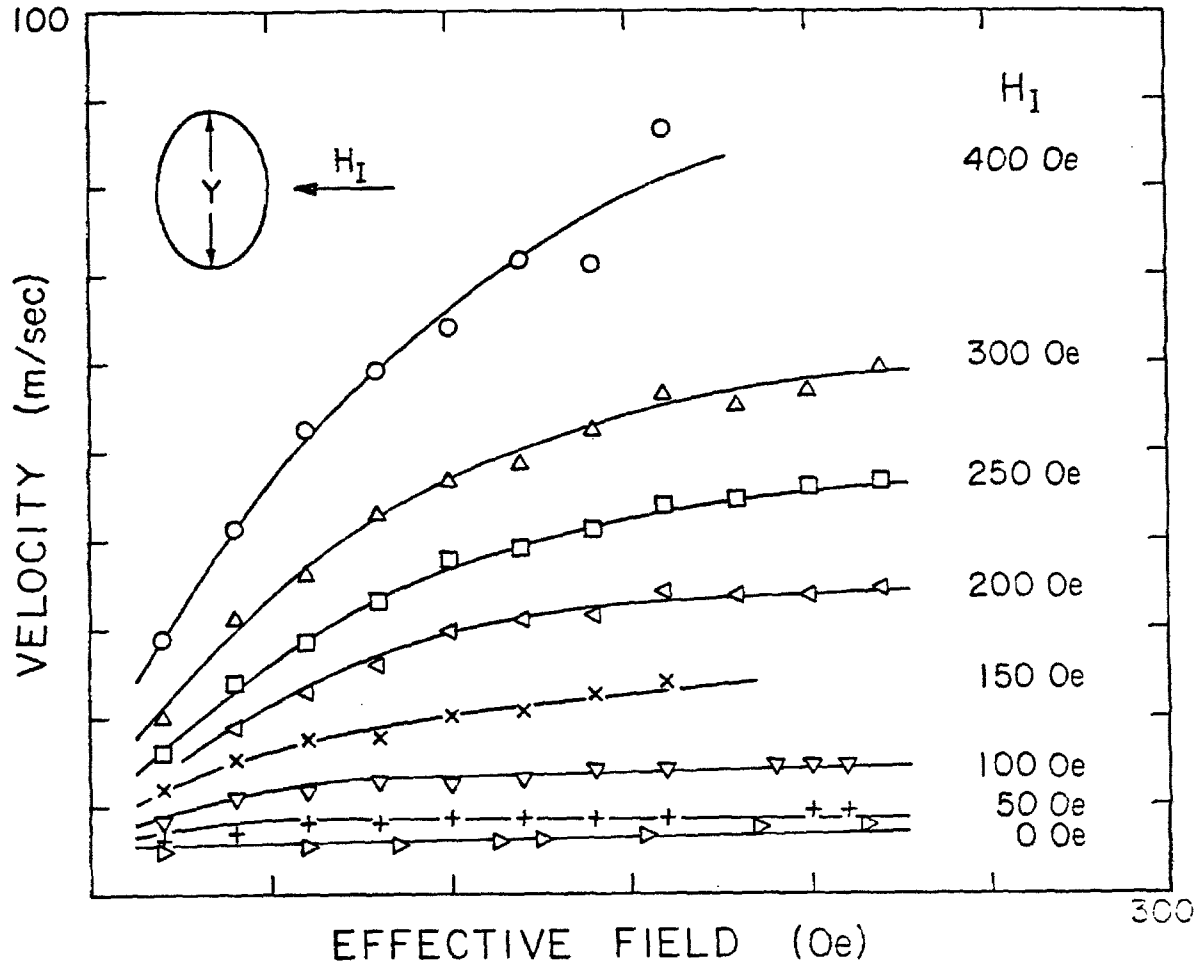

Figure 2,9, Average bubble radial velocity as a function of the effective drive field with the in-plane field along the wall as a parameter. Each point is an average of two to five bubbles.

in magnitude from 5.4 m/sec at H_{ix} = 0 to 8.6 m/sec at H_{ix} = 50 Oe and to 13 m/sec at 100 Oe. For $H_{ix} \geq$ 150 Oe v_s is still increased by the in-plane field but now a drive dependent velocity region is more clearly seen before a saturation is established. The in-plane field increases the non-linear mobility in the drive dependent velocity region. It also increases the drive threshold necessary for the velocity to saturate. For very high in-plane fields (H_{ix} = 400 Oe) the region of saturation velocity if it exists is higher than the drive range investigated here.

The average velocity of the wall is shown as a function of the in-plane field along the wall with the effective field as a parameter in Fig. (2.10). This method of presenting the data more clearly shows the role of the in-plane field. As can be seen the in-plane field does not affect the velocity at low magnitudes, $H_{ix} \leq$ 50 Oe, and the drive field does not have much effect in this range either. As the in-plane field is increased the velocity increases and becomes approximately linearly proportional to the H_{ix} for $H_{ix} \geq$ 150 Oe. The effect of the drive field in this range is to enhance the slope of the curves in addition to increasing the velocity. For example the slope increases from 0.12 m/sec-Oe to 0.27 m/sec-Oe when

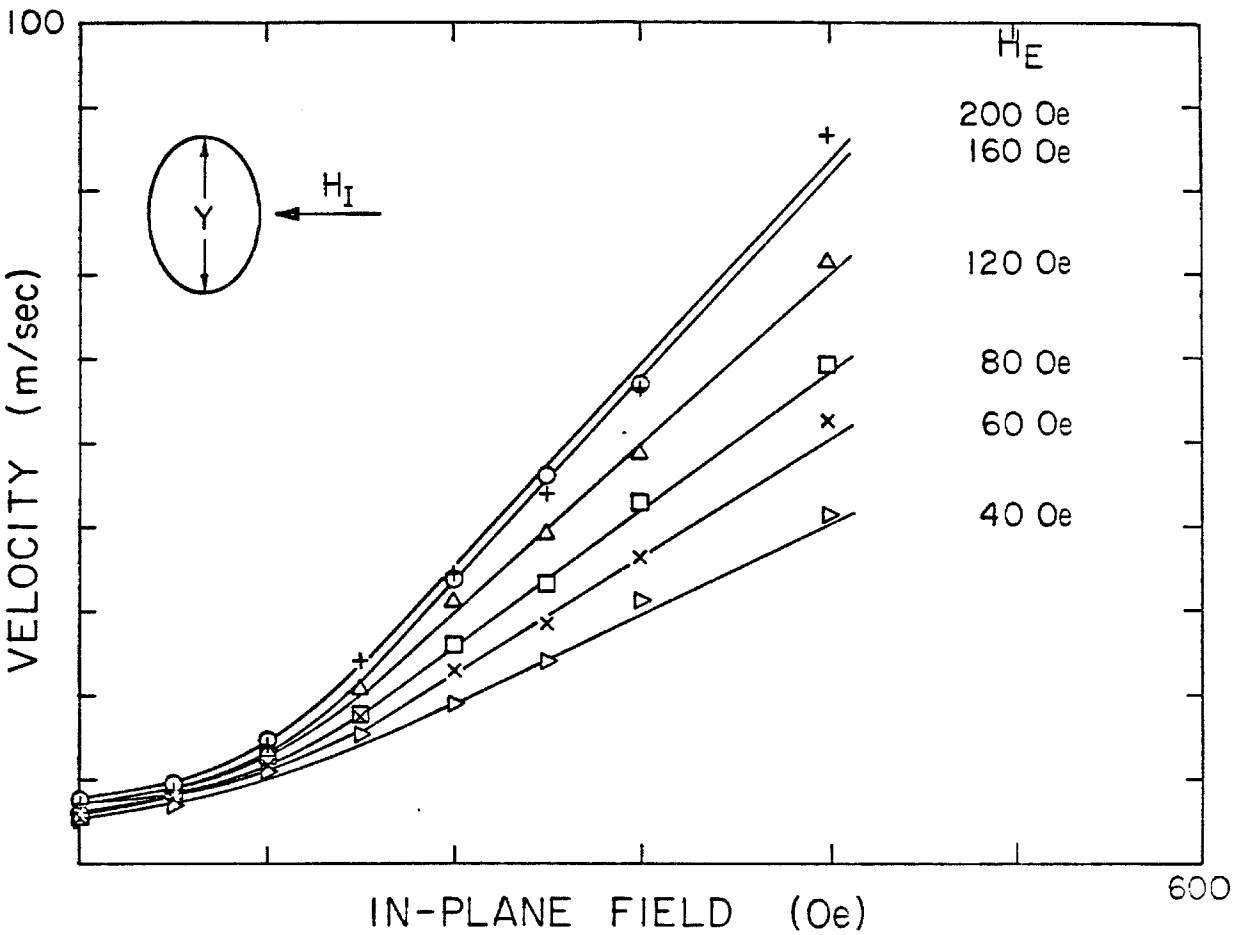

Figure 2.10. Average bubble radial velocity as a function of the in-plane field along the wall with the effective field as a parameter.

H_e is increased from 40 Oe to 200 Oe.

Wall Normal to the In-plane Field

The bubble radial distance as a function of time is shown in Fig. (2.11) for three different pulse fields with an in-plane field of H_{iy} = 100 Oe applied normal to the wall. The magnitudes of the pulse fields are (a) 90 Oe (b) 140 Oe and (c) 220 Oe. The observations are qualitatively the same as for the wall along the in-plane field. The velocity is saturated for this magnitude of in-plane field. The magnitude of the saturation velocity (8.5 m/sec) on the other hand is lower with respect to the wall along the in-plane field (13 m/sec). This anisotropy in the velocity is evident from the elliptical shape of the bubbles.

The bubble radial distance as a function of time is shown in Fig. (2.12) for three different pulse fields with an in-plane field of H_{iy} = 300 Oe. The pulse fields are (a) 75 Oe (b) 135 Oe and (c) 200 Oe. Here the domain wall moves with a wide structure, for all three pulse fields. In the crossed polarizer mode the dynamic wall looks wider than the observed static wall width. The position of the wall at any instant is defined as the midpoint of this wide boundary. Here the velocity is of interest and the structure of the wall will

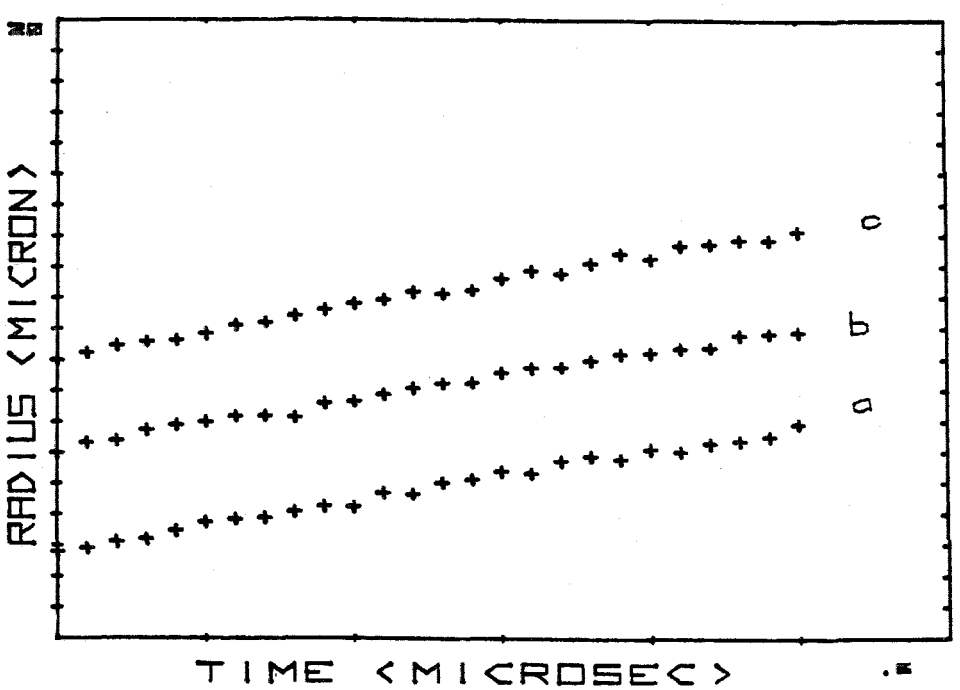

Figure 2.11. The bubble radius measured as a function of time with an in-plane field applied normal to the wall, H_{iy} = 100 Oe. The pulse fields used are (a) 90 Oe (b) 140 Oe (c) 220 Oe.

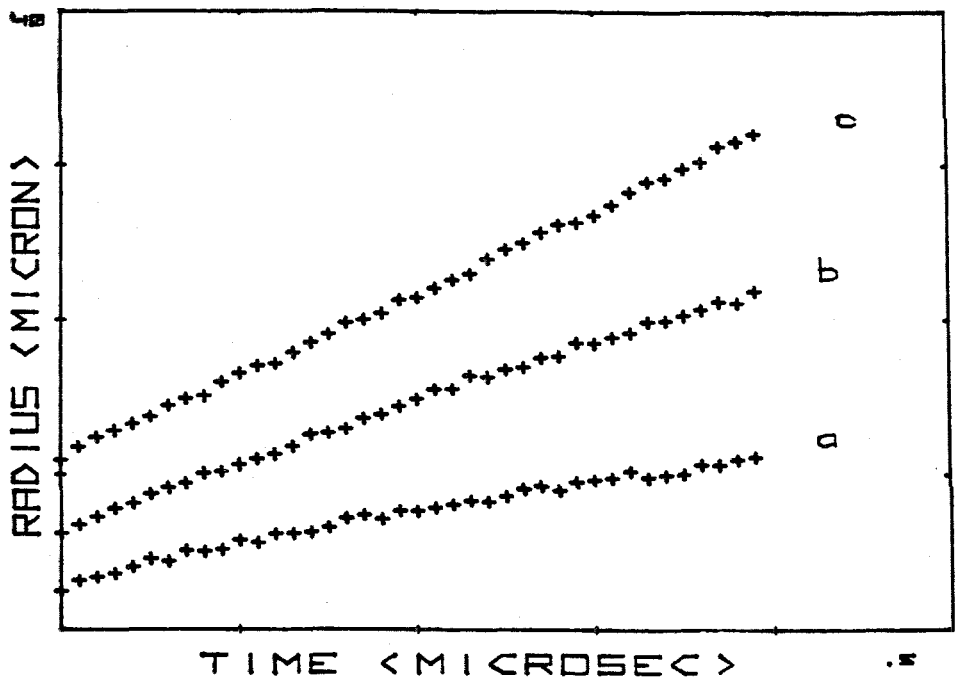

Figure 2.12. The bubble radius measured as a function of time with an in-plane field applied normal to the wall, H_{iy} = 300 Oe. The pulse fields used are (a) 75 Oe (b) 135 Oe (c) 200 Oe.

be studied in detail in Chapter 3. The results are qualitatively similar to the wall along the in-plane field case as in Fig. (2.7). The drive field increases the velocity and at H_p = 200 Oe there is saturation velocity, $v_s \sim 57$ m/sec, the same value as for the wall along the in-plane field. At this value of drive field the velocity anisotropy between the walls along and normal to the in-plane field is not present and the bubble is circular.

The average velocity of the wall is shown as a function of the effective field with an in-plane field applied normal to the wall as a parameter as shown in Fig. (2.13). The line crossing the data shows the threshold of the wide wall structure. It indicates the drive needed to visually detect a widening in the wall compared to its static width. The important features of the figure are qualitatively similar to the case of the wall along the in-plane field (Fig. 2.9) although the velocities are lower and above the threshold the wall structure is distinctly different. At low in-plane fields ($H_{iy} \leq 100$ Oe) the velocity is saturated and the in-plane field increases the saturation velocity. It is increased from 5.4 m/sec at H_{iy} = 0 to 6 m/sec at H_{iy} = 50 Oe and to 8.5 m/sec at H_{iy} = 100 Oe. As the in-plane field is increased a drive dependent velocity region is observed before saturation and at higher in-plane fields, H_{iy} = 400

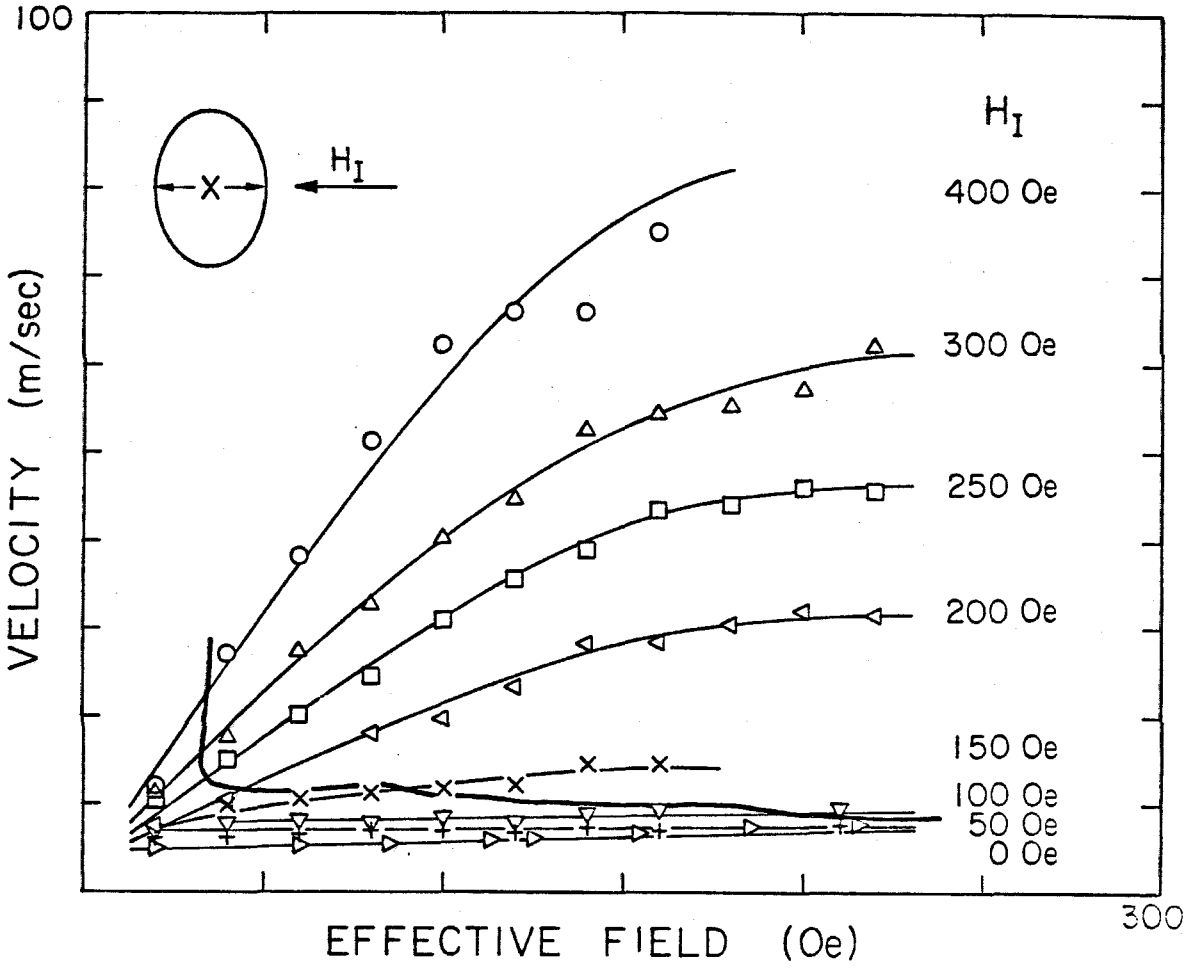

Figure 2.13. Average bubble radial velocity as a function of the effective drive field with the in-plane field normal to the wall as a parameter. The line crossing the data signifies a wall structure change threshold for higher fields.

Oe, saturation is not seen. The in-plane field enhances the non-linear mobility in the drive dependent region.

The average velocity of the wall normal to the in-plane field is shown as a function of the in-plane field, with the effective drive field as a parameter in Fig. (2.14). The line across the data is the same threshold shown in Fig. (2.13). The relative effects of the in-plane field and effective field on this threshold are better seen when the velocity is plotted this way. For in-plane fields below the threshold, the velocity is relatively insensitive to changes in the in-plane field however, above the threshold the velocity increases sharply and is essentially linearly proportional to the in-plane field. Above the threshold the slope is drive field dependent and is increased as the drive field increases. This increase becomes smaller for high fields, and the slope is constant for $H_e \geq 160$ Oe.

The radial wall motion along and normal to the in-plane field shows different velocity characteristics. The velocity of the wall along the in-plane field is generally higher than the one normal to it and the bubble expands elliptically. This is apparent at $H_i \leq 100$ Oe where both walls move with a saturation velocity, with v_s of the wall parallel to H_i, being 20-50% greater than the v_s of the wall perpen-

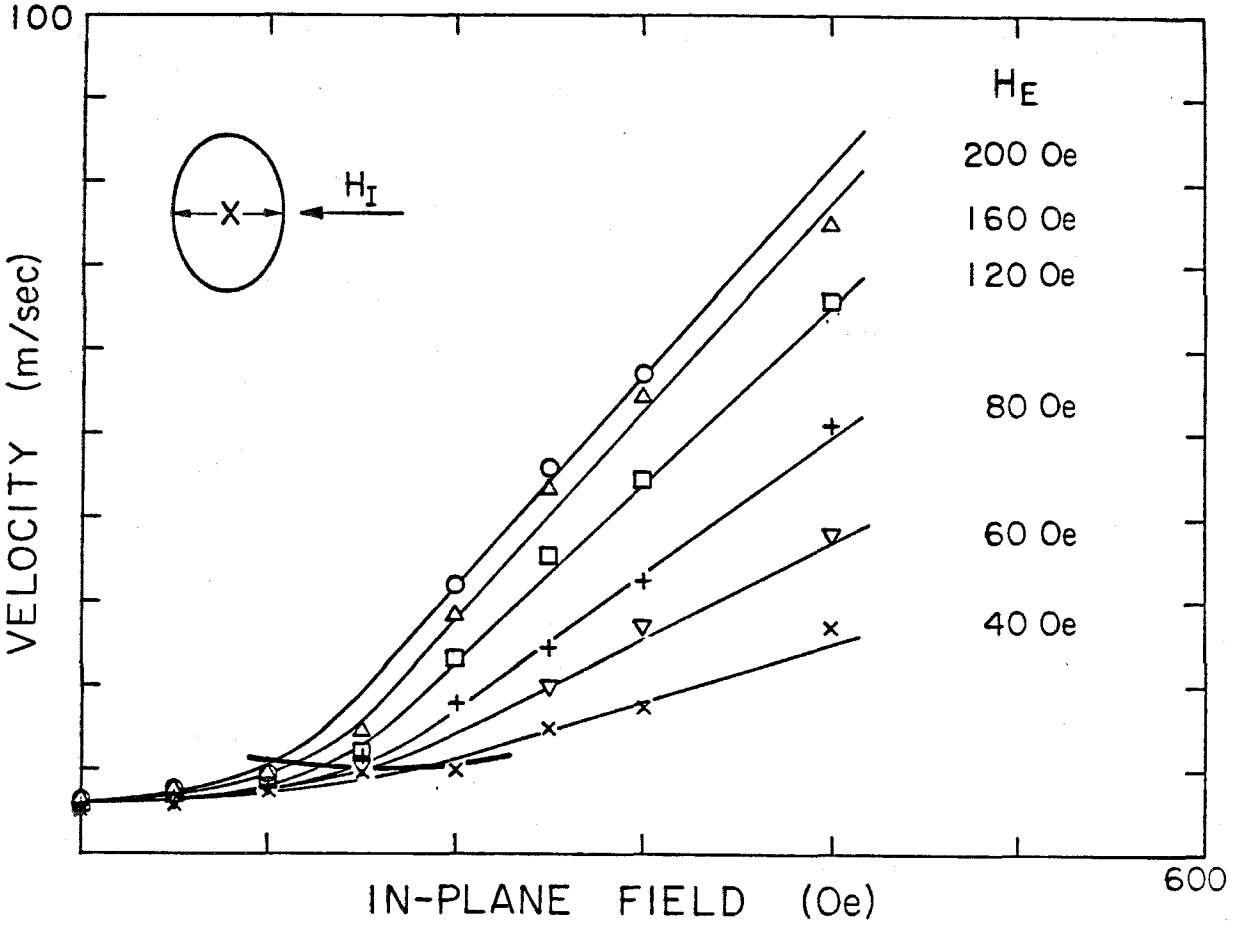

Fig. 2.14. Average bubble radial velocity as a function of the in-plane field normal to the wall with the effective field as a parameter. The line crossing the data signifies a wall structure change threshold for higher fields.

dicular to H_i. At high in-plane fields and high drives this velocity anisotropy disappears, making the dynamic bubble shape circular.

Conclusion

High drive field dynamics with an in-plane field show a saturation velocity at low in-plane fields. The in-plane field increases v_s. For higher in-plane fields a drive dependent velocity region is observed and saturation occurs at higher drive fields. At low H_i's the velocity is not affected by H_i and at high H_i's the velocity is linearly proportional to H_i. There is velocity anisotropy and the wall along the in-plane field generally has a higher velocity than the one normal to it.

REFERENCES

1. A. P. Malozemoff and J. C. Slonczewski, Magnetic Domain Walls in Bubble Materials (Academic Press, 1979).
2. J. C. Slonczewski, Int. J. Magn. 2, 85 (1972).
3. C. Kittel and J. K. Galt, Solid State Physics, ed. by F. Seitz and O. Turnbull (Academic Press, New York, 1956).
4. S. Chikazumi,Physics of Magnetism (John Wiley and Sons, Inc., New York, 1964).
5. T. H. O'Dell, Phys. Stat. Sol. (a) 48, 59 (1978).
6. J. D. Jackson, Classical Electrodynamics (John Wiley and Sons, Inc., New York, 1975).
7. E.Schlömann, J. Appl. Phys. 45, 369 (1974).
8. A. Hubert, J. Appl. Phys. 46, 2276 (1975).
9. A. H. Bobeck, Bell Sys. Tech. J. 46, 1901 (1967).
10. L. Landau and E. Lifschitz, Physic A. Sowjetunion 8, 153 (1935).
11. W. F. Brown, Micromagnetics (Interscience, New York, 1963).
12. T. L. Gilbert, Phys. Rev. 100, 1243 (1955).
13. L. R. Walker, unpublished. An account of this work is given in J. F. Dillon, Magnetism, ed. Rado and Suhl (Academic Press, New York, 1963).

14. H. C. Bourne and D. S. Bartran, IEEE Trans. MAG-8, 741 (1972).

15. N. L. Schryer and L. R. Walker, J. Appl. Phys. 45, 5406 (1974).

16. T. J. Gallagher and F. B. Humphrey, J. Appl. Phys. 50, 7856 (1979).

17. E. Emure, T. Fujii, S. Shiorni, and S. Uchiyama, IEEE Trans. Magn. MAG-3, 1169 (1977).

18. J. C. Slonczewski, J. Appl. Phys. 44, 1759 (1973).

19. B. E. McNeal and F. B. Humphrey, IEEE Trans. MAG-15, 1272 (1979).

20. K. Vural and F. B. Humphrey, J. Appl. Phys. 50, 3583 (1979).

21. F. B. Humphrey, IEEE Trans. MAG-11, 1679 (1975).

22. G. J. Zimmer, L. Gal, K. Vural and F. B. Humphrey, J. Appl. Phys. 46, 4976 (1975).

CHAPTER 3

Wall Deformation in Bubble Garnet Materials

The domain wall has been assumed to be straight through the thickness of a bubble thin film, statically and dynamically. The effect of the non-uniform fields, from the divergence of magnetization on the surfaces, was considered only on the internal structure of the wall. This assumption is reasonable to the first order; however, when large drive fields are present for long times, the situation is quite different and one should suspect that the rigid plane wall assumption would not apply. Certainly, the effects of the non-uniform fields on the configuration of the wall through the thickness must be taken into account and the rigid wall assumptions examined.

3.1 Stationary Wall Bulging

The demagnetizing field at the wall, in the z direction, is non-uniform [1] through the thickness in a bubble domain as shown in Fig. (3.1). Here the normalized z component of the demagnetizing field is shown as a function of normalized position, within the film at the bubble wall for a bubble where $r_o = h/2$. The field is calculated by integrating over the surface divergence of magnetization, similar

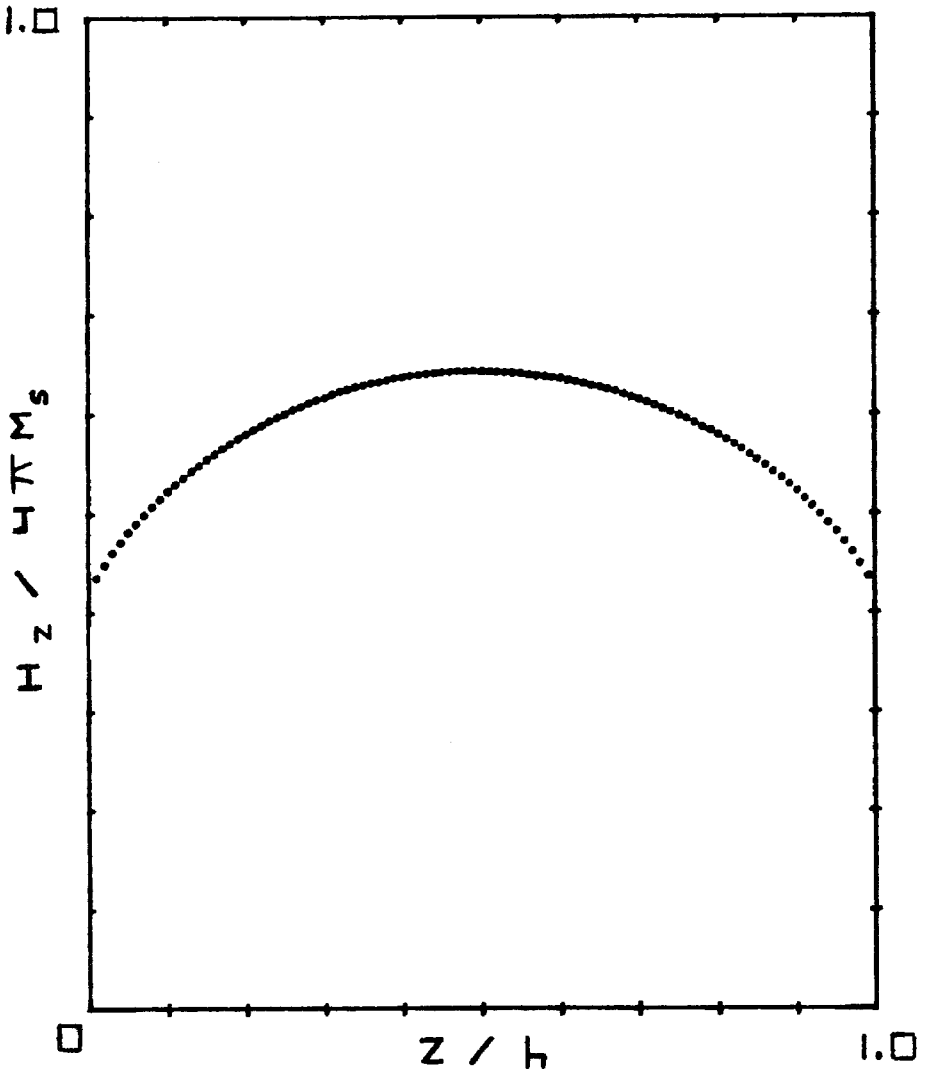

Figure 3.1. The demagnetizing field in the z direction in units of $4\pi M_s$ as a function of position through the thickness in units of h for a bubble with $r_o = h/2$.

to the procedure in finding the stray fields normal to the wall plane. As seen the field is higher by 0.2 ($4\pi M_s$) in the middle of the thickness compared to near the surfaces for a bubble with a diameter equal to the thickness. This is a typical size for a static bubble in garnet materials. This non-uniformity of the field decreases as the bubble radius increases and it is uniform for $r_o/h \geq 5$. It can be seen that the non-uniformity, as would be expected, is symmetric about the middle of the thickness.

The stationary bubble domain wall in the presence of this non-uniform demagnetizing field is slightly bulged [1-3] through the thickness. This bulge is shown qualitatively in Fig. (3.2). Here the magnitude of the bulge is exaggerated to emphasize the shape of the wall. One qualitative way to appreciate the effect of the non-uniform field is to think of the bubble radius as a function of the effective field in sections through the thickness of the film. The effective field is the difference between the uniform bias field and the local demagnetizing field at the thickness. It is low in the middle of film thickness making the radius large compared to near the surfaces where the effective field is high and the radius is small. The bulge is symmetric. The exact shape and magnitude of the bulge

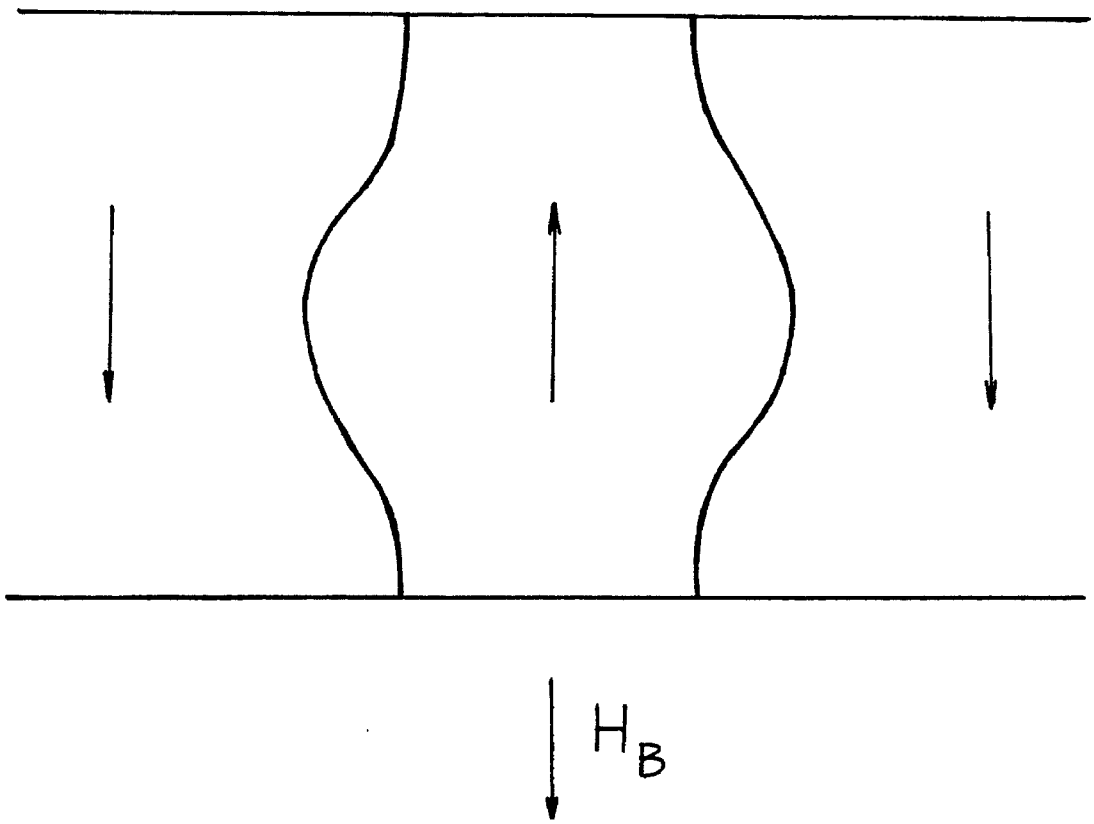

Figure 3.2. Stationary wall bulging for a bubble domain. The magnitude of the bulge is exaggerated to emphasize the shape of the wall. The wall is normal to the surfaces due to boundary conditions.

is determined by other effective fields generated as a result of the bulge and the boundary conditions near the surfaces. Numerical calculations [3] show that, for typical bubble films, the actual magnitude of the bulge is small, about 3% of the bubble radius.

A deformed wall has a higher total energy, assuming that the energy per unit area remains the same, because of the larger surface area compared to a plane wall. This added energy can be considered as a local effective surface tension field [4-5] generated in a direction opposing the deformation of the wall. This effective field depends on the local energy difference, at a point on the wall, due to the deformation there. For a smooth deformation, the effective surface tension field is

$$H_{ST} = \frac{2\sqrt{AK}}{M_s} \cdot \frac{1}{r_c} \qquad (3.1a)$$

where

$$r_c = \frac{[1 + (\frac{dq}{dz})^2]^{3/2}}{\frac{d^2q}{dz^2}} \qquad (3.1b)$$

is the radius of curvature of the deformation and q(z) is the distance between the bulged wall and the xz plane at

$y = 0$. Due to the surface tension field the magnitude of the bulge is reduced and the shape of the wall is smoother between the surfaces.

Deformations of the wall at the film surface are restricted by boundary conditions that require the bubble wall be normal to the film surface thus putting an inflection point in the wall shape between the surface and middle of the thickness. It is assumed that there is no surface anisotropy and that the crystal is strain free. The direction of the magnetic moments right at the surface and the ones directly below them have to be the same. Otherwise there would be an exchange torque present on the moments at the surface. Unless there is any surface anisotropy, this torque cannot be balanced out. Hence, equilibrium between the moments near the surface is possible only when they are parallel. This boundary condition at the surface can be expressed as

$$\frac{d\bar{m}}{dn} = 0 \qquad (3.3)$$

This condition assumes that both exchange and anisotropy energies can be expressed as volume integrals without any

surface terms which is very reasonable for the system considered here. The same result can be obtained by using the transversality condition in calculus of variations [7]. As a result of this boundary condition the wall is normal to the surfaces and there is an inflection point in the wall shape between the surface and middle of the thickness as in Fig.(3.2).

3.2 Dynamically Deformed Wall Structure

For a moving wall to retain its static shape, all parts of the wall must have the same velocity. It was shown in Chapter 2 that the wall velocity is very sensitive to the effective in-plane field. Therefore the effective in-plane field profile through the thickness must be important in determining the dynamical shape of the wall. Fig. (2.4) showed the normalized effective in-plane field as a function of normalized position through the thickness. With an in-plane field of $H_i = 1.2(4\pi M_s)$ applied, Fig. (3.3a) is for the H_i normal to wall and Fig. (3.3b) is for the H_i along wall. As seen from Fig. (3.3a) for the field normal to wall, the stray fields add to H_i in $0 \leq z \leq h/2$ and subtract in $h/2 \leq z \leq h$. Therefore a large effective in-plane field difference ($2.24\ (4\pi M_s)$) is present within the film that is increased by an applied field normal to the wall. On the other hand when the field is along the wall, the applied

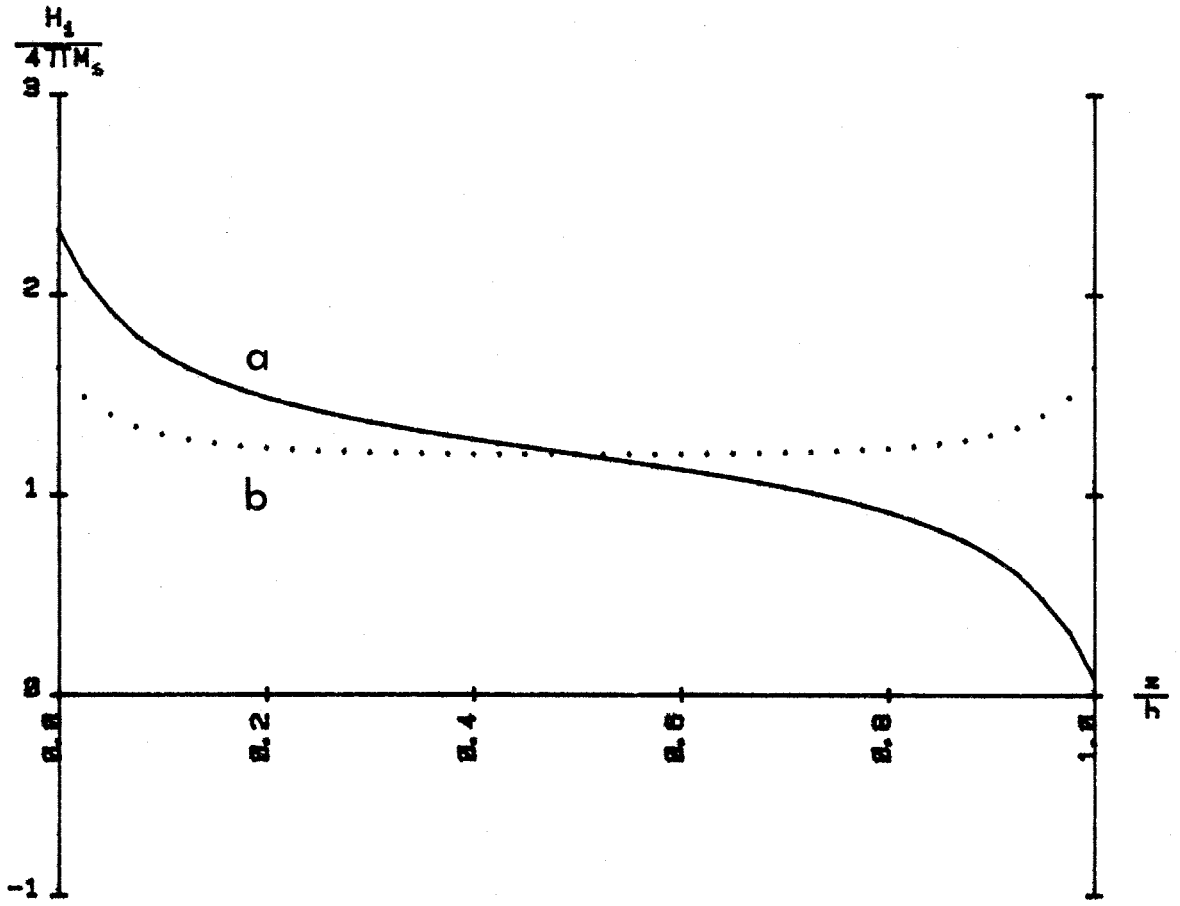

Figure 3.3. The effective in-plane field in units of $4\pi M_s$ as a function of position through the thickness in units of h for an in-plane field of magnitude $H_i=1.2(4\pi M_s)$, (a) normal to the wall (b) along the wall.

field is normal to the stray fields and the resultant magnitude of the effective in-plane field is more uniform as seen from Fig. (3.3b). The difference in the effective in-plane fields near the surfaces is small ($0.44(4\pi M_s)$).

The domain wall is deformed dynamically as a result of the non-uniform effective in-plane profile through the thickness. The mechanism for the deformation can be understood by using the results of Chapter 2 where it was shown that an in-plane field increases the velocity of a wall [8]. If we assume that different parts of the wall respond in relation to the magnitude of the effective in-plane field on them, there will be significantly different velocities through the thickness. The deformation, in turn, generates effective surface tension fields. The shape of the wall is finally determined by the functional dependence of velocity on the drive and in-plane field, the stray field profile, the surface tension fields and the fields applied externally.

The dynamic wall deformation can be simulated numerically. The wall through the thickness is divided into 20 segments. The effective drive and in-plane field on each segment is calculated every 0.5 nsec. The functional dependence of the velocity on the drive and in-plane field is taken phenomenologically as the results of Chapter 2. The

effective in-plane field profile through the thickness is calculated as in Fig. (3.3) for the segment and the decrease in the effective drive field is also taken into account. The surface tension fields generated due to deformations are calculated at each segment center by finding the radius of curvature there. The wall is normal to the surface at all times.

The growth of deformation of wall with time is shown in Fig.(3.4). Here the 200 Oe in-plane field is normal to the wall and the wall motion. The wall starts as a plane wall at the lefthand side of the figure at t=0. The curves thereafter represent the position of the wall at 40 nsec intervals for the first 400 nsec of wall motion. A 135 Oe pulse field is applied. The parameters of sample 2-16-44 are used along with its functional dependence of velocity on the in-plane and drive field characteristics obtained experimentally in Chapter 2. The direction of the applied in-plane field is such that it adds to the stray fields near the top surface. Hence the velocity of the wall is higher there compared to the lower surface where the stray fields subtract from the applied in-plane field. This velocity difference results in the deformation of the wall with the shape as in Fig. (3.4).

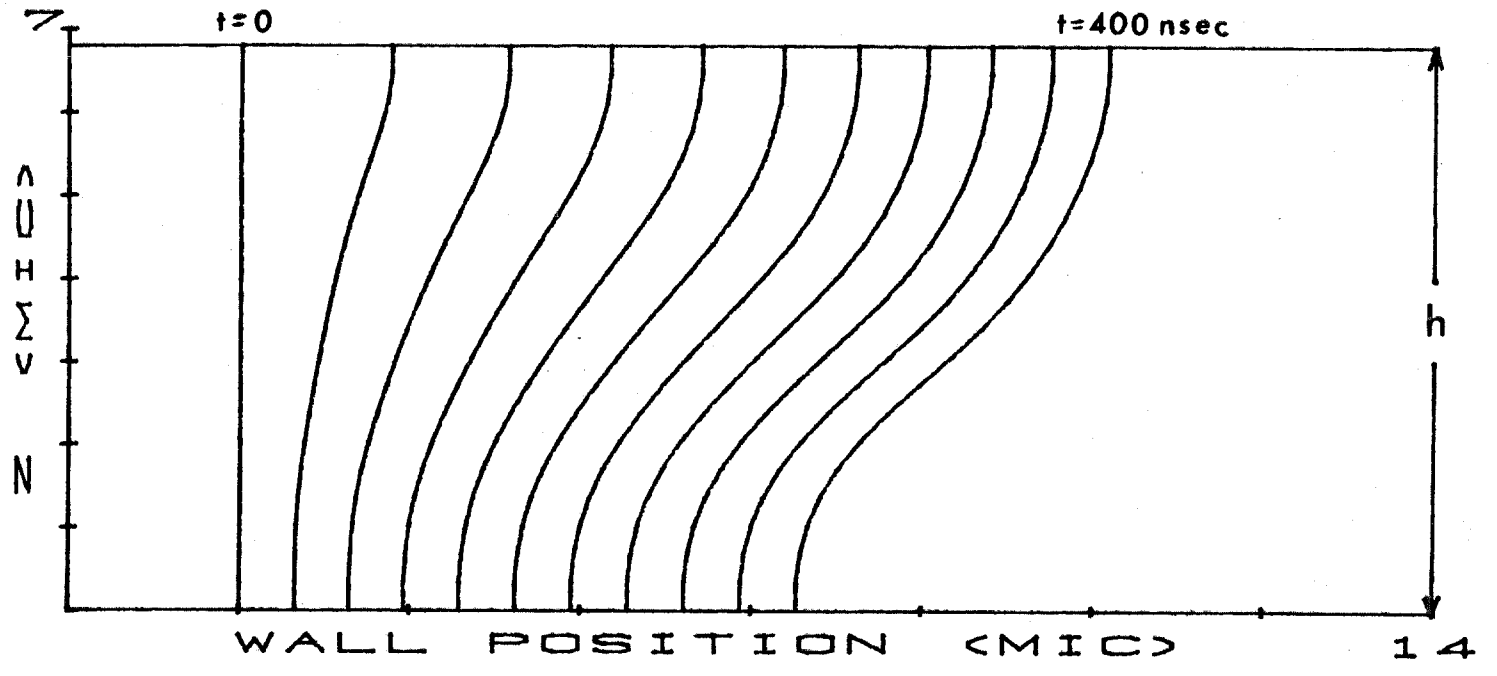

Figure 3.4. The position of the wall through the thickness in microns as a function of position normal to the wall plane in microns at 40 nsec intervals drawn by computer simulation for the sample 2-16-44. A 400 nsec, 135 Oe pulse field is applied in the presence of a 200 Oe in-plane field normal to the wall.

The rate of change of the wall deformation width goes to zero with time as shown in Fig. (3.5). Here the difference in position between the leading and trailing edges of the deformed wall in microns is shown as a function of time in nsec using the computer simulation for sample 2-16-44. The same fields are used as in Fig. (3.4). As seen the rate of change of width decreases with time and is nearly constant after 220 nsec. As the wall deforms surface tension fields are generated due to the curvatures. The direction of these fields for the parts of the wall near the upper surface is opposite to the drive field. Hence, the drive field decreases with time on the leading edge as a result of the combination of bubble effective field decrease and the generation of surface tension fields. The leading edge is in the drive field dependent region, having a high effective in-plane field on it, and its velocity drops with time. On the other hand the changes in the effective drive field do not affect the trailing edge much since it has a low effective in-plane field on it and is in the saturation velocity region. The decrease in the velocity difference between the leading and trailing edges cause the width to saturate as in Fig. (3.5).

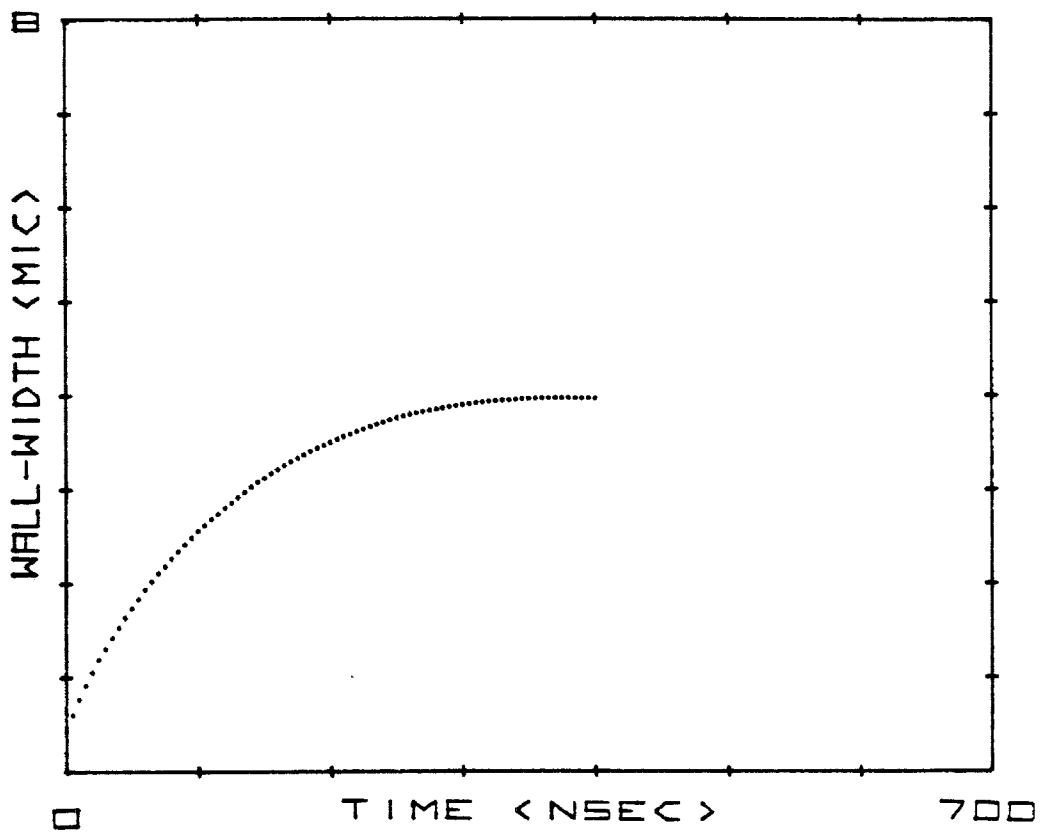

Figure 3.5. The width of the deformation in microns as a function of time in nsec drawn by computer simulation for sample 2-16-44. A 400 nsec, 135 Oe pulse field is used in the presence of a 200 Oe in-plane field normal to the wall.

3.3 Dynamically Deformed Wall in Bubble Garnet Materials

The direction of the fields used in experiments with respect to the bubble domain in garnet material is shown in Fig. (3.6). The applied in-plane field is from left to right. The stray field directions at the surfaces are shown for the static wall. The resultant effective in-plane field is shown on the dynamic wall at the lefthand side. The characteristics of the samples used in the experiments are shown in Appendix C.

Transient pictures with 10 nsec exposure time of an expanding bubble in the presence of an in-plane field are shown in Fig. (3.7). Fig. (3.7a) is taken in the transmission (Faraday) mode at the film-substrate interface. Both pictures are taken in the crossed polarizer mode. The small circle in the center is the bubble photographed before the pulse field is applied and is in equilibrium with the bias field of 68 Oe. It has a diameter of 5.8 μm which provides a scale for the pictures taken at the same magnification. An in-plane field of 200 Oe is applied. The directions of the fields are as in Fig. (3.6) with the Kerr mode used to observe the upper surface. The pictures are taken 200 nsec after the application of a 190-Oe expanding pulse field. The bismuth containing sample H280 was used. Both pictures are of the sample under identical conditions. The observed "width" of the wall caused by diffraction of the light by the

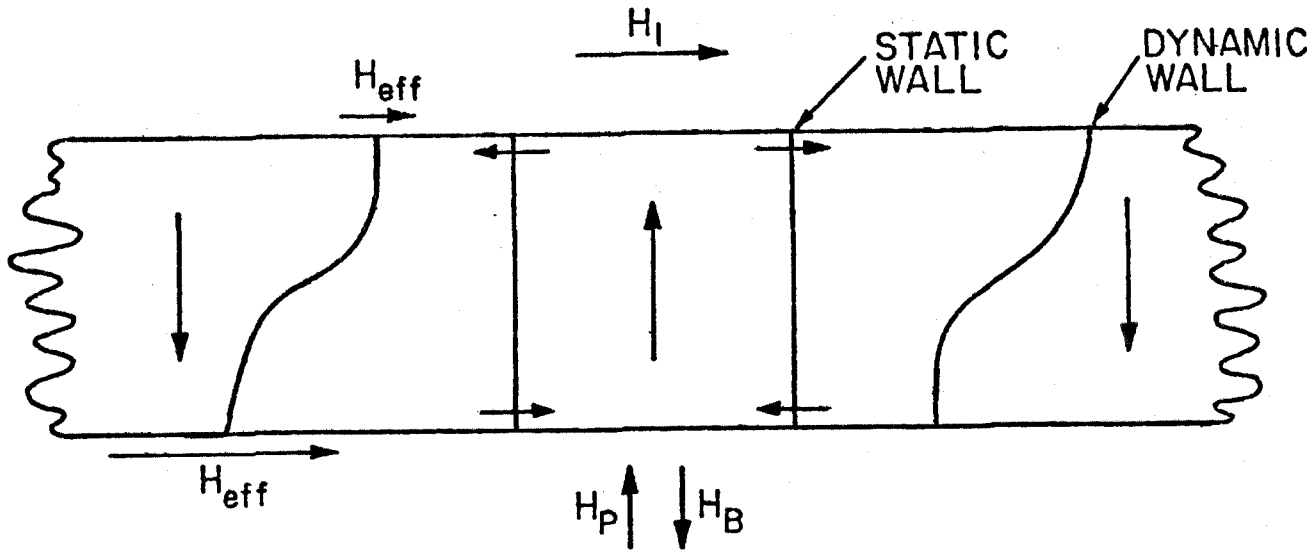

Figure 3.6. The direction of the fields used in experiments with respect to the bubble domain in garnet material. The top surface is the film-substrate interface.

Figure 3.7 Bubble domain 200 nsec after a 190-Oe 300-nsec expanding pulse as seen (a) in the transmission mode and (b) in the reflection mode at the film-substrate interface. The small circle in the middle is the bubble in equilibrium with the bias field and has a diameter of 5.8 μm. An in-plane field of 200 Oe is applied from left to right and a bias field of 68 Oe is applied into the page. Bi-containing sample H-280 is used.

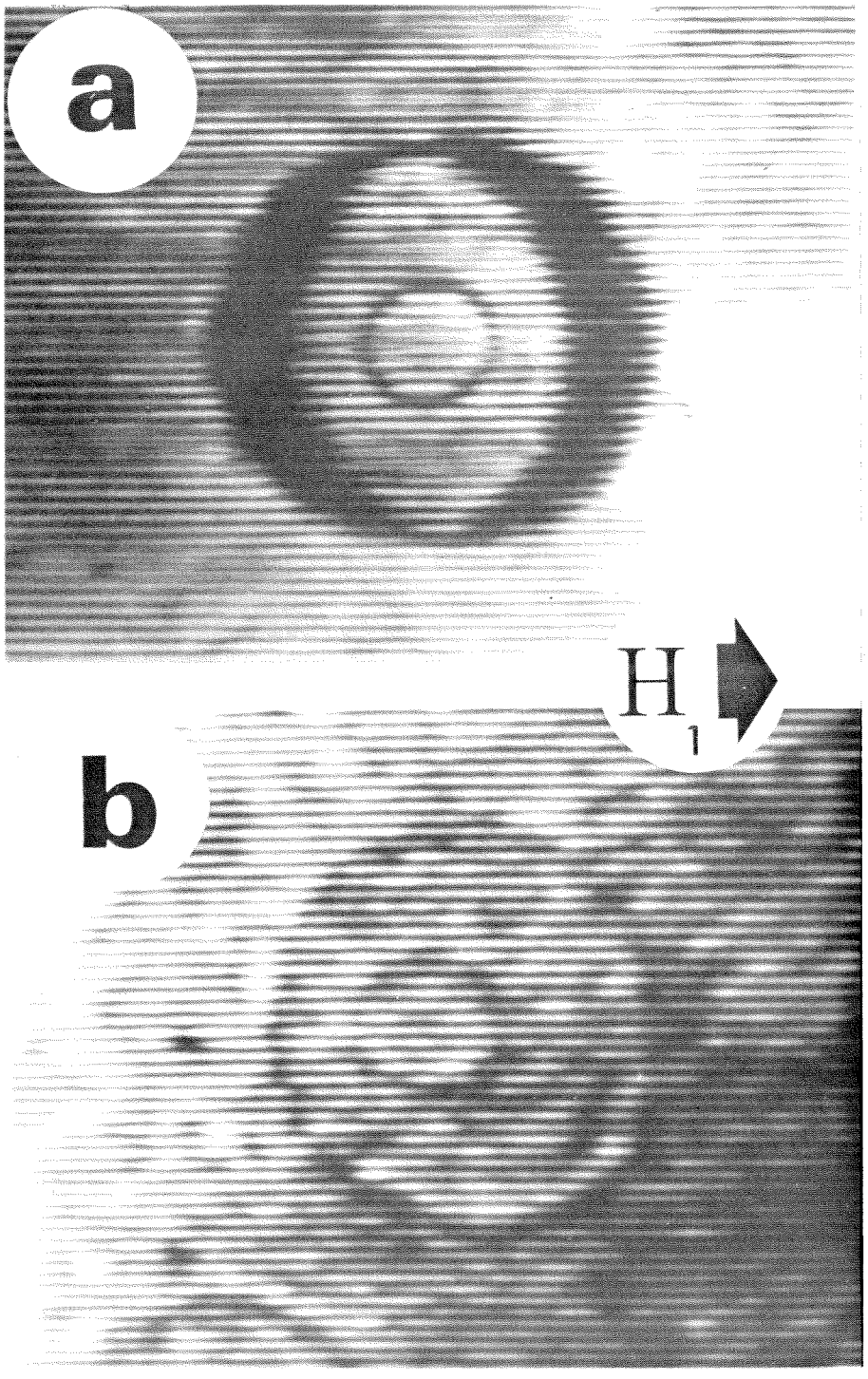
a
H1
b

wall can be seen from the static bubble pictures in both modes. The calculated width from the sample parameters is 0.1 μm, while the observed width is 0.8 μm. In transmission [Fig. (3.7a)] the wall normal to the in-plane field shows a distinctly wide structure since it is deformed due to the velocity differences through the thickness. The observed width of the wall, that is the difference between the leading and trailing edges, is largest at the point where H_i is normal to the bubble wall since the effective in-plane field differences through the thickness are largest there. The contrast across the wide wall is fairly uniform as a result of the structure shown by computer simulation in Fig. (3.4). The wall edges are rather sharp transition regions confirming that the wall is normal to the surfaces as required by the boundary conditions. The dynamic width of that portion of the wall that is parallel to the in-plane field has hardly changed with respect to the static wall width, however, since there are not large enough effective in-plane field differences, as shown in Fig. 3.3, to cause deformations through the thickness for this wall.

The velocity anisotropy near the surfaces in the bubble domain wall can be seen from Fig. (3.7b). Here the dynamic wall width is the same as the static wall since the part of the wall only near the surface is observed. The wall moving

in the direction of the in-plane field (right wall in picture) has a higher velocity than the one moving opposite to it (left wall). This is as a result of the stray fields adding to the H_i for the right wall and subtracting for the left wall. The difference in the positions of the two walls with respect to the static bubble at the point where the walls are normal to the in-plane field is equal to the wall width seen in transmission mode Fig. (3.7a). No difference in the velocities between the two portions of the wall that are moving normal to the in-plane field are seen in the reflection mode since the effective in-plane field is the same for both.

The film-substrate interface shows results similar to the film-air interface. The contrast, however, is poor. Also the sample is necessarily farther away from the pulse coil (the substrate is in between the film and coil) so that only a limited range of drive pulses could be used. Even with these difficulties, it is clear that the observations made at the film-substrate interface are representative of both film surfaces. Reversing the direction of the in-plane field or the bias field interchanges the characteristics of the slow and fast walls that are seen in Fig. (3.7b), i.e., the static bubble is closer to the right side of the dynamic bubble. This kind of reversal is

consistent with the model and, in many ways, is just as appropriate as looking at the other interface.

A quantitative comparison of the position of the wall as seen in transmission and reflection modes has been made. The position of the leading and trailing edge of the wall seen in transmission (□) and the wall position seen in reflection (X) as a function of time after the application of a 190 Oe expanding pulse is shown in Fig. (3.8). The position is measured along a line through the bubble center parallel to the 200 Oe in-plane field. Sample H280 was used biased at 68 Oe with the Kerr reflection from the film-substrate interface. Fig. (3.8a) is for the walls moving in the direction of the in-plane field corresponding to the right wall in Fig. (3.7) and Fig. (3.8b) is for the walls moving in the direction opposite to the in-plane field corresponding to the left wall. It can be seen in Fig. (3.8a) (for the right side) that the leading edge in transmission has the same position as the wall in reflection. The agreement is very good, well within experimental error. Similarly it can be seen from Fig. (3.8b) (for the left side) that the trailing edge in transmission has the same position as the wall in reflection. The characteristics of both the walls moving along and opposite to the in-plane field in transmission are similar. The leading edge is

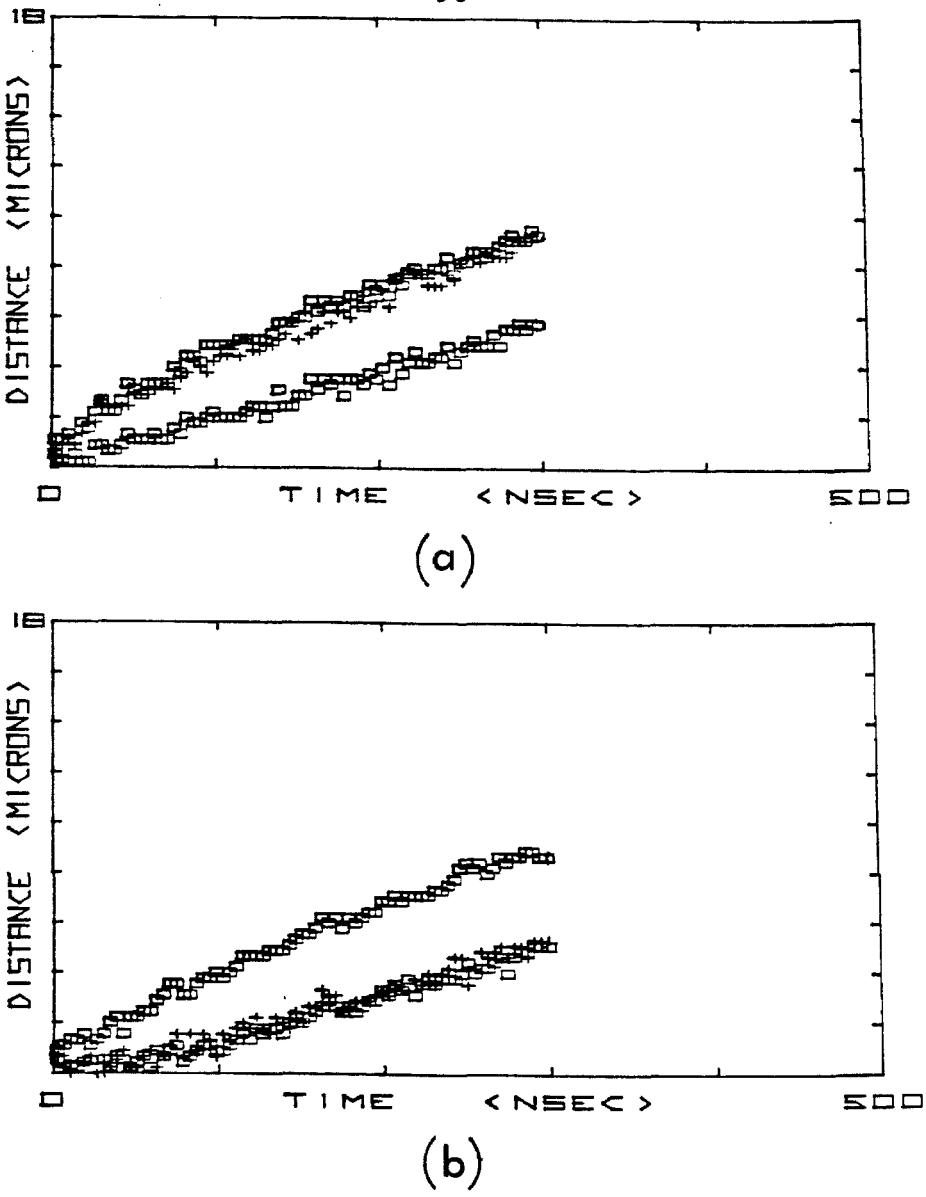

Figure 3.8 The position of the leading and trailing edge of the wall seen in the transmission mode (□) and in the reflection mode (+) as a function of time after the application of a 190 Oe 300 nsec expanding pulse for (a) the wall moving in the direction of H_i and (b) the wall moving opposite to H_i. The in-plane field is 200 Oe with a bias field of 68 Oe in the bismuth containing sample H280.

faster than the trailing edge initially, having a high effective in-plane field on it. The velocity difference between the two edges decreases with time since surface tension fields due to deformations develop and the bubble effective field decreases.

The growth of the dynamic deformation can be seen by measuring the difference in the positions of the leading and trailing edges at various times. Fig. (3.9) shows the apparent wall width in transmission mode plotted as a function of time for sample 2-16-44. The wall width for the wall moving in the direction of the 200 Oe in-plane field is shown (+) as well as in the opposite direction (□). A 135 Oe 400 nsec pulse field was used with a bias field of 80 Oe. Measurements were done every 2 nsec. As can be seen, both walls behave in the same way. The width increases at a rate of 20 m/sec up to 150 nsec and then the rate of change drops to an essentially constant saturation width similar to as shown in Fig. (3.5) using computer simulation. The occurrence of a saturation width is typical of all the samples studied at high drive and in-plane fields.

The magnitude of the deformation is influenced by both the drive and in-plane fields. The saturation wall width as a function of the in-plane field with the pulse

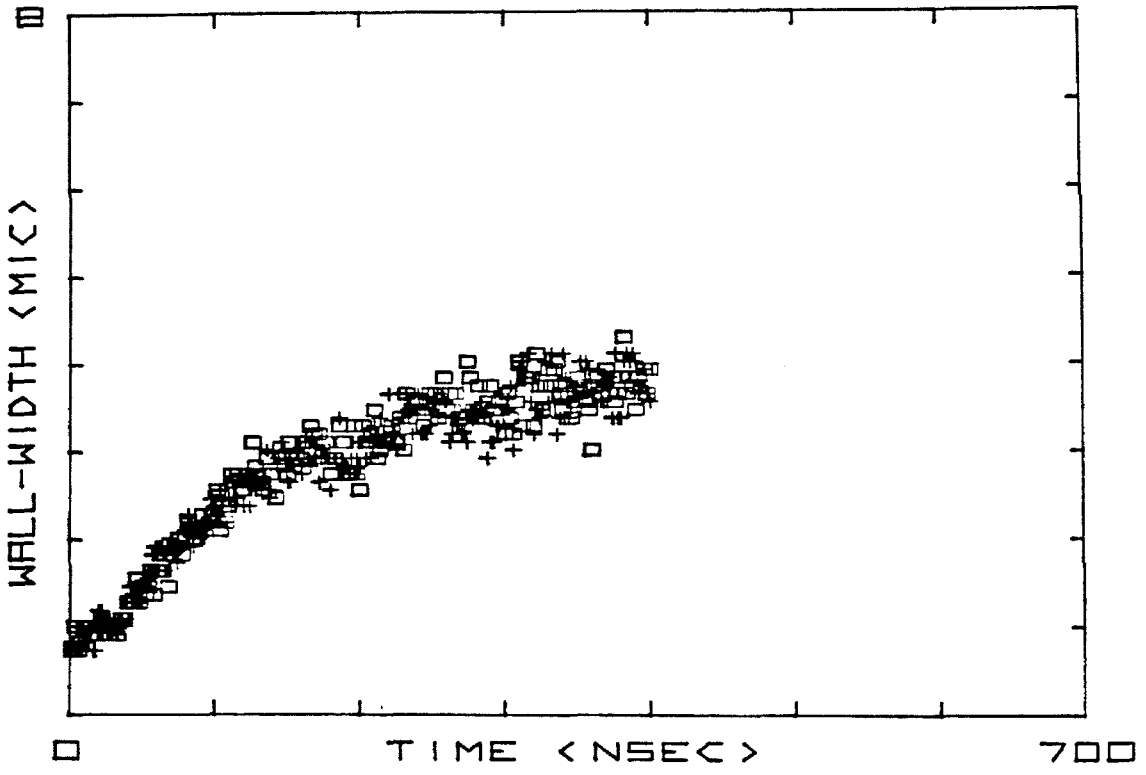

Figure 3.9 The apparent wall width as a function of time for the wall moving in the direction of H_i (+) and opposite to the H_i (□). A 135 Oe 400 nsec pulse field is used along with an in-plane field of 200 Oe and a bias field of 80 Oe in sample 2-16-44.

field as a parameter is shown in Fig. (3.10) for the as-grown sample 2-16-44. There is a region of low in-plane fields when the wall is narrower than the observed static wall width of 0.8 μm but presumably, wider than the calculated equilibrium value 0.1 μm. Once the deformation is experimentally detected, the in-plane field as well as the pulse field increases its width. When the drive field is increased, the leading edge velocity is enhanced since its drive dependence is high, having a high effective in-plane field on it. The trailing edge velocity, on the other hand, does not change appreciably since its drive dependence is low, having a low effective in-plane field on it. An increase in the drive field, therefore, enhances the velocity difference between the two edges causing the width to increase. Similarly an increase in the applied in-plane field at a constant drive increases the effective in-plane field on the leading edge and enhances its velocity. The trailing edge still has a low effective in-plane field on it and its velocity is not changed much. Hence increasing the in-plane field enhances the velocity difference between the two edges, increasing the width. At higher in-plane fields the width becomes less in-plane field dependent as in Fig. (3.10). The trailing edge in this case has a high effective

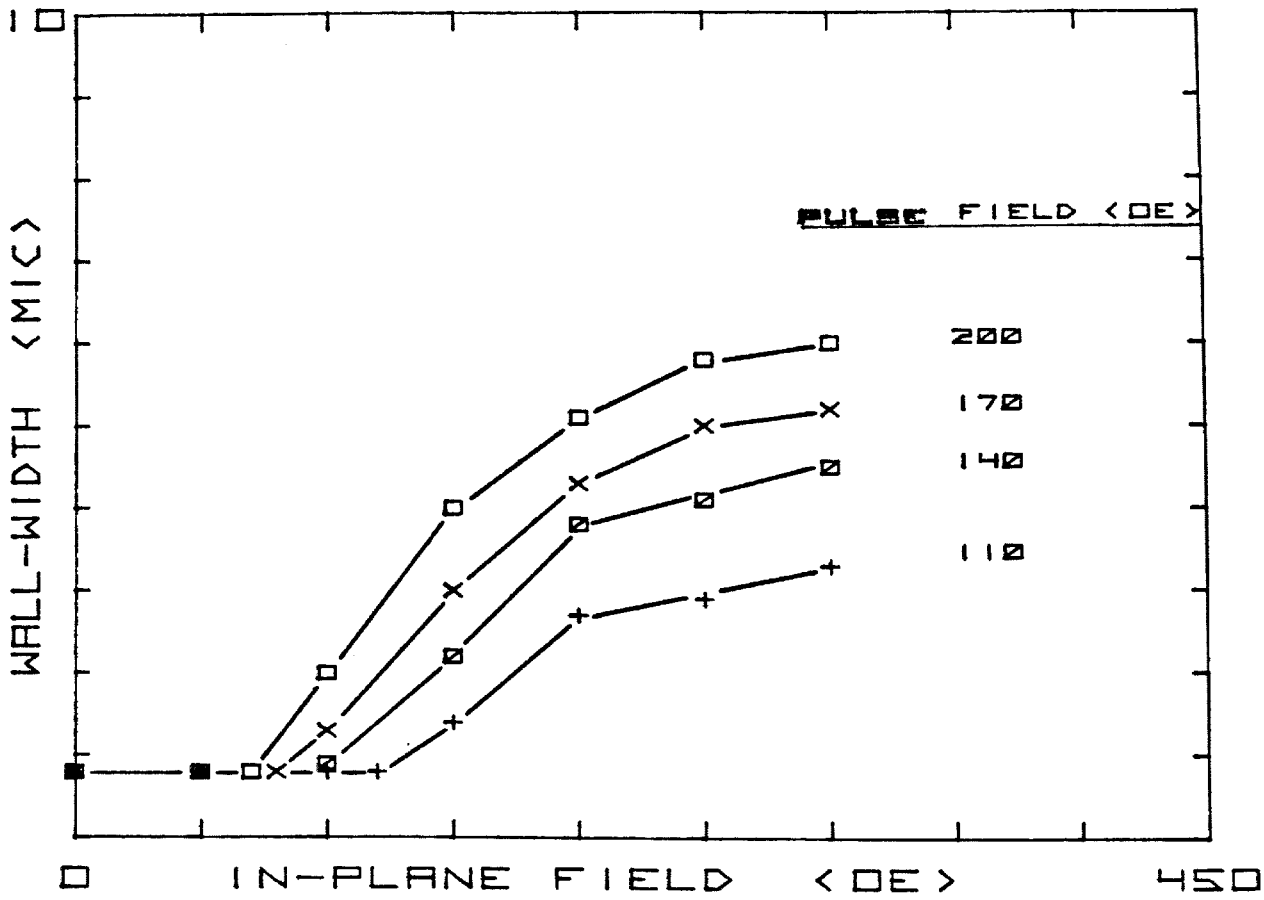

Figure 3.10 The wall width as a function of the in-plane field with the pulse field as a parameter for sample 2-16-44.

in-plane field on it and its velocity increases similarly as the leading edge with in-plane field.

The ease of forming the deformation depends on the anisotropy. Three samples with different anisotropy and otherwise similar parameters have been investigated. The threshold for detection of the deformation as a function of in-plane field and pulse field is shown in Fig. (3.11). For this experiment, the pulse field is held at a constant value while the in-plane field is increased until wall widening is just detected. As can be seen, lower pulse and in-plane fields are required to establish the deformed structure in samples with a smaller anisotropy field. The surface tension field opposes the drive field on the leading edge and decreases its velocity, causing the wall width to saturate. Since the magnitude of this field is lower in samples with a low anisotropy, smaller drive fields are required to form observable widths. If the anisotropy is low enough, the velocity difference between either surface and the middle of the sample just due to the stray field profile can be high enough to see the deformation without an applied in-plane field as in samples LPED-252 and Un-335. In this case the wall deforms symmetrically about the mid-plane of the sample with the parts of the wall near the surfaces having a higher velocity.

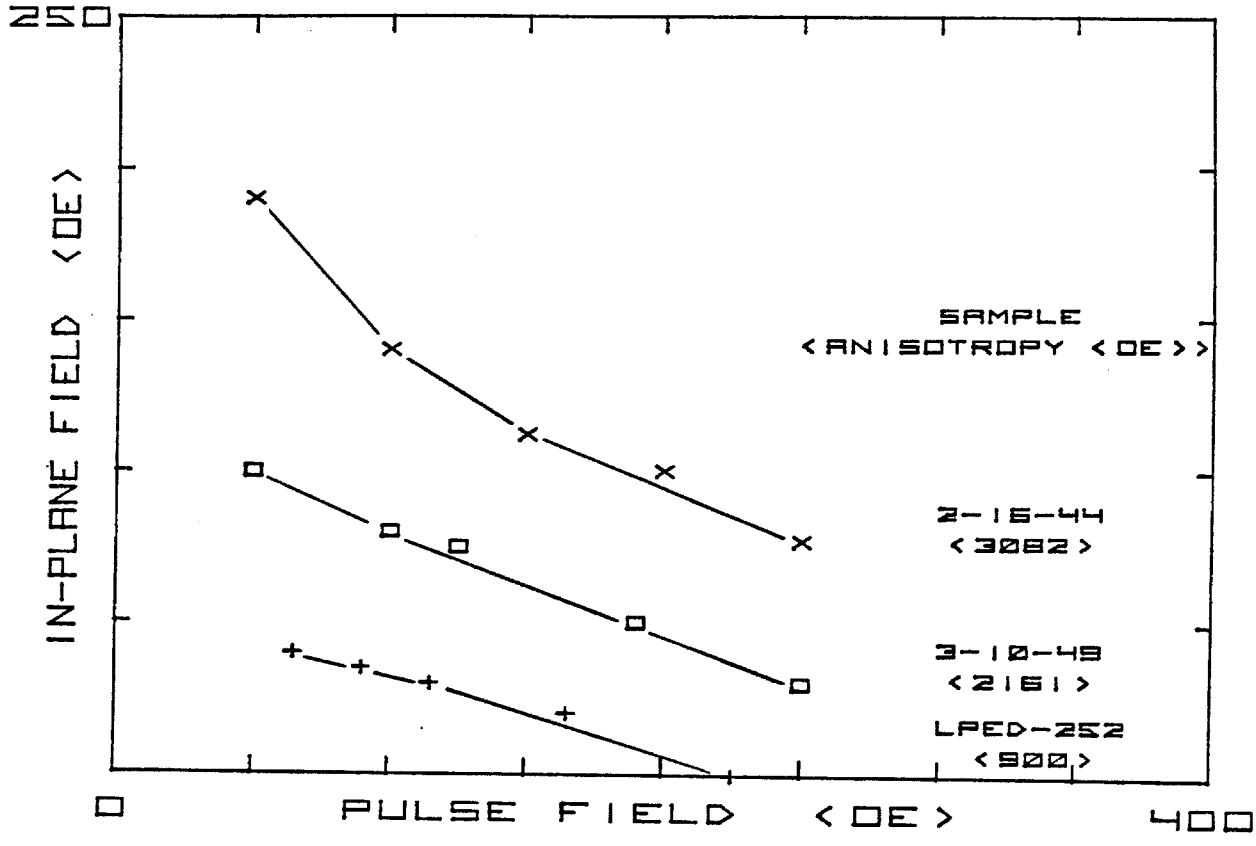

Figure 3.11 The threshold for the detection of the deformation as a function of the in-plane field and pulse field for three samples with different anisotropies.

Conclusion

The domain wall is dynamically deformed at high drive and in-plane fields. The mechanism for the deformation is based on the spatial variations of in-plane fields at the wall through the film thickness, due to the addition of the stray fields at the film surfaces and the applied in-plane field. This causes different parts of the wall to move with different velocities. The deformed wall can be studied in the bulk of the film by transmission (Faraday) mode and at the surfaces by reflection (Kerr) mode. Both the drive field and the in-plane field enhance the wall width due to the functional dependence of the wall velocity near the surfaces on these fields. It is easier to form the structure in samples with a lower anisotropy since the surface tension field opposing the deformations is lower in these samples.

REFERENCES

1. A. A. Thiele, Bell Syst. Tech. J. 48, 3287 (1969).
2. G. M. Nedlin, J. Appl. Phys. 50, 2204 (1979).
3. T. G. W. Blake and E. Della Torre, J. Appl. Phys. 50, 2192 (1979).
4. J. C. Slonczewski, Int. J. Magn. 2, 85 (1972).
5. A. P. Malozemoff and J. C. Slonczewski, Magnetic Domain Walls in Bubble Materials (Academic Press, New York, 1979).
6. W. F. Brown, Magnetostatic Principles in Ferromagnetism (North-Holland, Amsterdam, 1962).
7. A. R. Forsyth, Calculus of Variations (Cambridge University Press, London, 1927).
8. K. Vural and F. B. Humphrey, J. Appl. Phys. 50, 3583 (1979).
9. F. B. Humphrey, IEEE Trans. Magn. MAG-11, 1679.

APPENDIX A

Static Properties of Bubble Domains

The size and stability of cylindrical magnetic domains will be considered here [1-3]. Fig. A-1 shows the domain configuration and the coordinate system used. The circular domain is an isolated unperturbed bubble while the perturbed one (in dashed lines) is shown as having a three-fold symmetry. The bubble is magnetized down while in the rest of the material, extending to infinite dimensions, it is magnetized up. The material is uniaxial and the z axis is taken along the easy axis which is normal to the sample. The origin of the cylindrical coordinate system (r,θ,z) used, is in the center of the bubble. The domain wall is assumed to have zero width and to be straight through the thickness. The wall interacts with the component of the applied field only in the z direction. The saturation magnetization M_s is constant everywhere and is always in the z direction. The model is most accurate for materials with $K_u >> 2\pi M_s^2$.

The bubble size and stability are determined by taking the first and second variations with respect to the radius in the total energy of the system. The radius of the bubble is described by the expansion

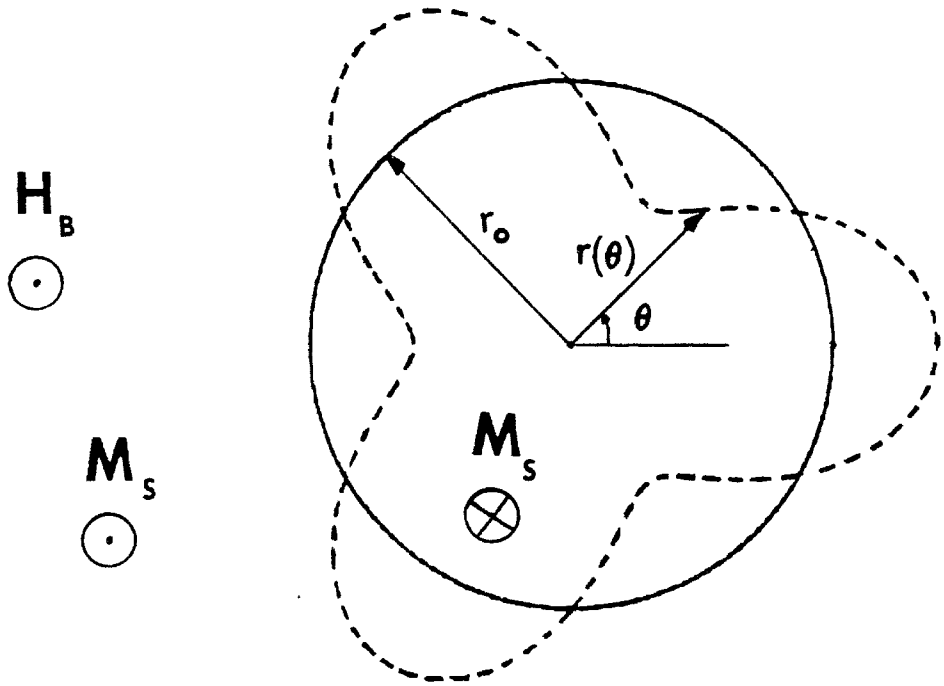

Figure A-1. Domain configuration and coordinate system used in stability and size calculations.

$$r_b(\theta) = r_o + \Delta r_o + \sum_{n=1}^{\infty} \Delta r_n \cos[n(\theta - \theta_n - \Delta\theta_n)] \qquad (A\text{-}1)$$

and the variations in the energy are taken with respect to r_n and θ_n. The circular bubble is defined by $r_b(\theta) = r_o$ and it is assumed that the variations in the radius are small compared to r_o. The total energy of the system consists of three terms. The wall energy (E_w), the externally applied field energy (E_H) and the magnetostatic energy (E_M). The total energy is

$$E_T = E_w + E_H + E_M$$

The wall energy per unit area, σ_w, is taken to be constant and independent of the wall orientation or curvature. The total wall energy is given by

$$E_w = \int_a \sigma_w \, da = h\sigma_w \int_0^{2\pi} \{r_b^2(\theta) + [\frac{\partial r_b(\theta)}{\partial \theta}]^2\}^{1/2} \, d\theta \qquad (A\text{-}2)$$

where a is the wall area and the total wall energy is found by integrating the arc length around the circumference of the bubble and multiplying it by the height. The wall energy is less when size of the domain is reduced. For a circular domain, i.e., $r_b(\theta) = r_o$ and $\frac{\partial r_b(\theta)}{\partial \theta} = 0$

the variations are

$$\left(\frac{\partial E_w}{\partial r_o}\right)_o = 2\pi h\ \sigma_w \tag{A-3}$$

$$\left(\frac{\partial^2 E_w}{\partial r_n^2}\right)_o = \frac{\pi}{r_o}\ h\ \sigma_w\ n^2 \qquad n \geq 1 \tag{A-4}$$

where the subscript zero means the derivatives are taken when the domain is circular. The derivatives not written explicitly are equal to zero.

The externally applied field energy (E_H) is given by

$$E_H = -\int_V \bar{M}\cdot\bar{H}\ dv = hM_sH \int_0^{2\pi} r_b^2(\theta)\ d\theta - \text{const} \tag{A-5}$$

where the volume of the bubble determines the total energy and the constant is not important since the variations in the energy are considered here. The applied field energy is less when the size of the domain is reduced. For a circular domain

$$\left(\frac{\partial E_H}{\partial r_o}\right)_o = 4\pi r_o\ hM_sH \tag{A-6}$$

$$\left(\frac{\partial^2 E_H}{\partial r_o}\right)_o = 4\pi h\, M_s H \qquad \text{(A-7)}$$

$$\left(\frac{\partial^2 E_H}{\partial r_n^2}\right)_o = 2\pi h\, M_s H \qquad n \geq 1 \qquad \text{(A-8)}$$

The magnetostatic energy (E_M) is due to the divergence of magnetization on the surfaces of the sample. It is the most difficult term to deal with because of the form of the equations. It is given by

$$E_M = \frac{1}{2} \int_V \int_{V'} \frac{\bar{\nabla}\cdot\bar{M}\ \bar{\nabla}'\cdot\bar{M}'}{|\bar{r}-\bar{r}'|}\, dv'\, dv \qquad \text{(A-9)}$$

This energy is reduced when the size of the domain is increased. For a circular domain

$$\left(\frac{\partial E_M}{\partial r_o}\right)_o = -\,(2\pi h^2)(4\pi M_s^2)\, F(d/h) \qquad \text{(A-10)}$$

$$\left(\frac{\partial^2 E_M}{\partial r_o^2}\right)_o = -\,(4\pi h)(4\pi M_s^2)\, \frac{\partial F(d/h)}{\partial (d/h)} \qquad \text{(A-11)}$$

$$\left(\frac{\partial^2 E_M}{\partial r_n^2}\right) = -(2\pi h)(4\pi M_s^2)\frac{\partial F(d/h)}{\partial(d/h)} \qquad \text{(A-12)}$$

$$+ h\,4\pi M_s^2 \frac{2r_o}{h}\left[L_n\left[\left(\frac{h}{2r_o}\right)^2\right] - L_n(o)\right] \quad \text{for } n \geq 1$$

where

$$F(x) = \frac{2}{\pi} x^2 \left\{\left(1+\frac{1}{x^2}\right)^{1/2} E\left[\left(1+\frac{1}{x^2}\right)^{-1}\right] - 1\right\} \qquad \text{(A-13)}$$

$$L_n(x) = \int_0^{\pi} \frac{(1-\cos n\alpha)\, d\alpha}{\left[x+\frac{1}{2}(1-\cos\alpha)\right]^{1/2}} \qquad x \geq 0 \qquad n \geq 0 \qquad \text{(A-14)}$$

where $x = \frac{d}{h}$ and $E\left[\left(1+\frac{1}{x^2}\right)^{-1}\right]$ is the complete elliptic integral of the second kind. $F(x)$ is called the force function.

First order derivatives $\left(\frac{\partial E_T}{\partial r_n}\right)_o$ and $\left(\frac{\partial E_T}{\partial \theta_n}\right)_o$ are all zero due to the rotational symmetry of the problem and only $\left(\frac{\partial E_T}{\partial r_o}\right)_o$ is not zero. The equilibrium condition is

$$\left(\frac{\partial E_T}{\partial r_o}\right)_o = 0 \qquad \text{(A-15)}$$

This is called the "force equation" from which the radius of the bubble for an applied field can be found. The

equation does not necessarily imply the stability of the domain.

Of the second order derivatives only $(\frac{\partial^2 E_T}{\partial r_n^2})_o$ are non-zero and these are called the stability coefficients of the system. The force equation can be used to eliminate the applied field terms from the second order derivatives to simplify the stability coefficients. The total energy variation can be written as

$$\frac{\Delta E_T}{2(4\pi M_s^2)(\pi h^3)} = \left[\frac{\ell}{h}+\frac{d}{h}\frac{H_b}{4\pi M_s} - F(\frac{d}{h})\right]\frac{\Delta r_o}{h}+\frac{1}{2}\left\{-(2\frac{h}{d})\left[\frac{\ell}{h}-s_o(\frac{d}{h})\right]\ (\frac{\Delta r_o}{h})^2\right.$$

$$\left. + \sum_{n=2}^{\infty}(n^2-1)(\frac{h}{d})\left[\frac{\ell}{h} - s_n(\frac{d}{h})\right]\ (\frac{\Delta r_n}{h})^2\right\} + 0(3) \qquad \text{(A-16)}$$

where $\ell = \frac{\sigma_w}{4\pi M_s^2}$ is the intrinsic length

and

$$S_o(\frac{d}{h}) = F(\frac{d}{h}) - d\frac{\partial}{\partial d}F(\frac{d}{h}) \qquad \text{(A-17)}$$

$$S_n(\frac{d}{h}) = \frac{1}{n^2-1}\left\{S_o(\frac{d}{h}) + \frac{1}{2\pi}(\frac{d^2}{h^2})\left[L_n(\frac{h^2}{d^2}) - L_n(o)\right]\right\} \qquad \text{(A-18)}$$

The force equation is obtained by setting the coefficients of $\frac{\Delta r_o}{h}$ to zero and we get

$$\frac{\ell}{h} + \frac{d}{h}\frac{H_b}{4\pi M_s} - F\left(\frac{d}{h}\right) = 0 \qquad \text{(A-19)}$$

The terms are the generalized forces with respect to the bubble radius and force per unit area is obtained by dividing the equation by πdh. The first term is proportional to the wall energy generating a force in a direction to decrease the bubble radius and the force per unit area is inversely proportional to the bubble diameter. The second term is proportional to the applied field and generates a force per unit area independent of the bubble diameter in a direction to reduce the bubble diameter when the field is along the directions of the magnetization outside the bubble. The third term generates an internal demagnetizing force per unit area and is proportional to the demagnetizing field on the wall averaged over the film thickness. It is in a direction to increase the radius. A stable bubble has the wall energy and applied field forces collapsing the bubble in equilibrium with the demagnetizing force expanding the bubble.

The domain diameter can be found as a function of the applied field graphically using the force equation once the

material parameters ℓ, $4\pi M_s$ and h are known. Fig. A-2 shows the graphs of $F(\frac{d}{h})$, $S_o(\frac{d}{h})$ and $S_2(\frac{d}{h})$. A straight line is drawn with a slope of $H_b/4\pi M_s$ intersecting the vertical axis at ℓ/h. It intersects F(d/h) at two points and these two points are the solutions to the force equation. The larger diameter is the radially stable solution (r_+) while the smaller diameter is radially unstable (r_-). This does not imply stability with respect to other modes of deformation in the radius (as in Fig. A-1). In terms of energy considerations the two solutions are extremums but for the larger diameter the bubble is in a potential maximum. When the applied field is increased the diameter of the unstable solution increases while the stable one decreases and they meet at the point where the straight line becomes tangent to the F(d/h). This is called the collapse field and no stable bubble solution exists for higher fields. Here the inward force proportional to the wall energy dominates all the other forces.

Stability is completely characterized by examining the signs of the coefficients of $(\frac{\Delta r_n}{n})^2$ (corresponding to the total energy second derivative). As seen from Equation A-16 for the sign of the coefficients to be positive

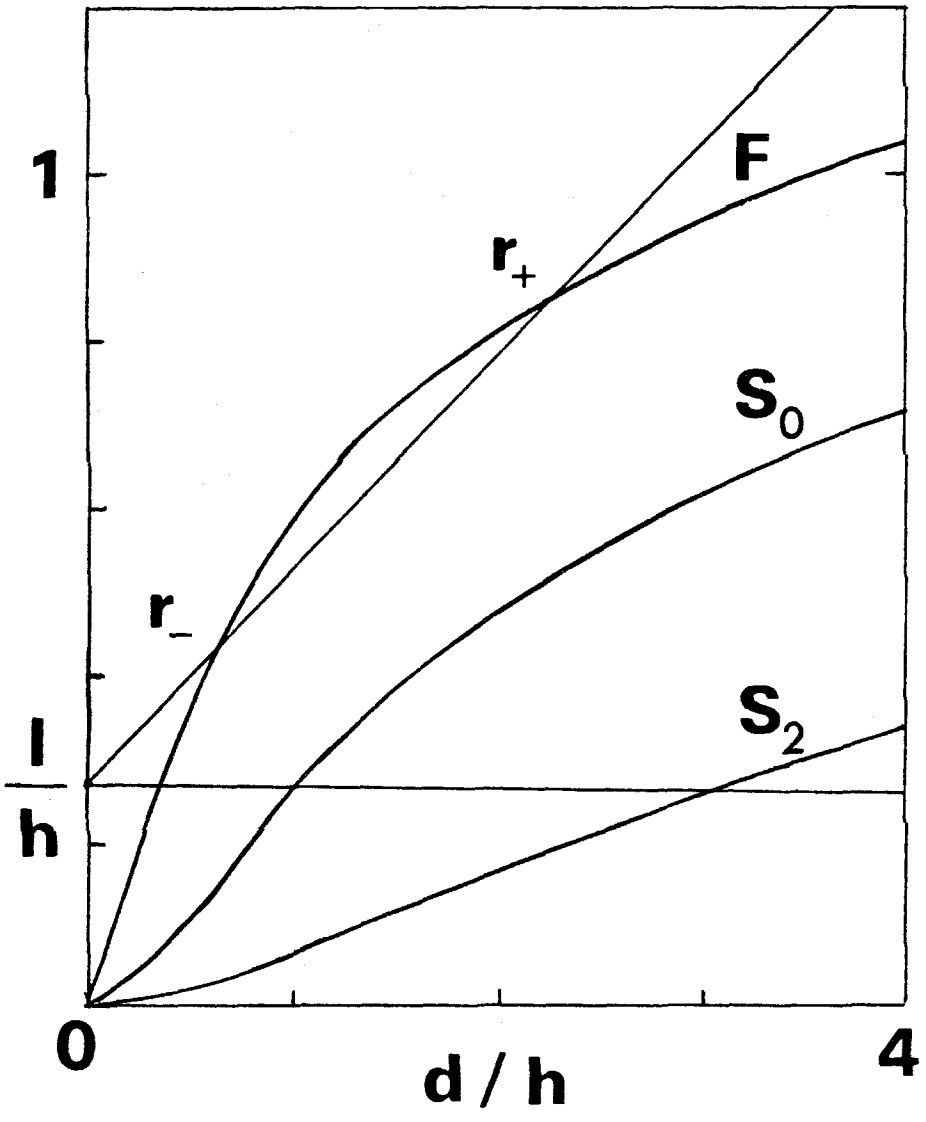

Figure A-2. The bubble force function F and stability function S_o and S_2 as a function of diameter in units of thickness. The intersection of the horizontal line (ℓ/h) with S_o and S_2 give the collapse and stripeout radii, respectively. The intersection of the straight line, with a slope $H_b/4\pi M_s$, with F gives the stable (r_+) and unstable (r_-) bubble radii.

$$S_o(\frac{d}{h}) > \frac{\ell}{h} > S_n(\frac{d}{h}) \quad n > 2 \tag{A-20}$$

and since

$$S_{n+1}(\frac{d}{h}) < S_n(\frac{d}{h}) \tag{A-21}$$

Equation A-20 reduces to

$$S_o(\frac{d}{h}) > \frac{\ell}{h} > S_2(\frac{d}{h}) \tag{A-22}$$

This condition is shown as the straight line with zero slope intersecting the vertical axis at ℓ/h. The bubble is stable in the region between points where this line intersects $S_o(\frac{d}{h})$ and $S_2(\frac{d}{h})$. The point where it intersects $S_o(\frac{d}{h})$ is called the collapse diameter (at collapse field - H_{co}) below which no stable bubble diameter is present. The point where the straight line intersects $S_2(\frac{d}{h})$ is called the stripeout diameter (at the stripeout field - H_{so}) above which the bubble domain transforms into a stripe domain.

The bubble radius as a function of the applied field can be seen in Fig. (A-3). The parameters of sample 2-16-44 are used. Both the stripeout (H_{so}) and collapse fields (H_{co})

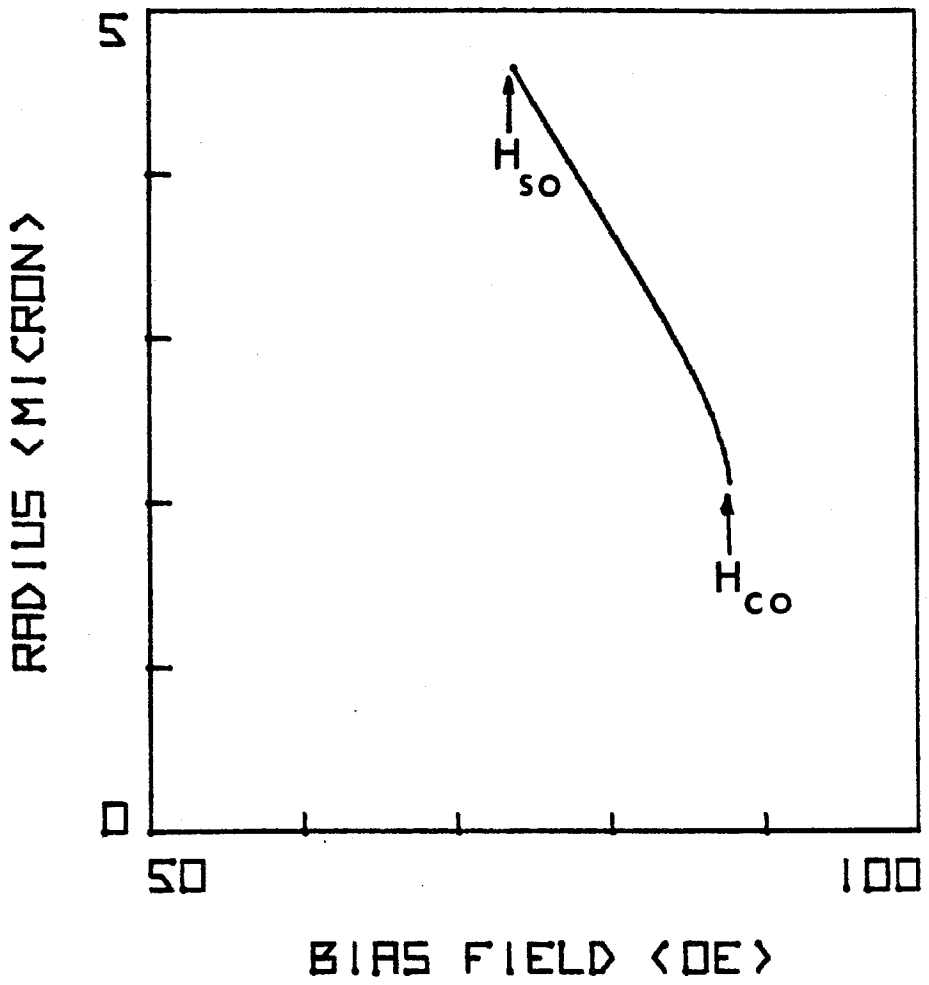

Figure A-3. The bubble radius as a function of the bias field for sample 2-16-44. The stripeout field (H_{so}) and the collapse field (H_{co}) are shown.

are shown. This curve is particularly useful to calculate the effective drive field change during bubble radial expansion.

REFERENCES

1. A. H. Bobeck, Bell Syst. Tech. J. 46, 1901 (1967).
2. A. A. Thiele, Bell Syst. Tech. J. 48, 3287 (1969).
3. A. A. Thiele, Bell Syst. Tech. J. 50, 725 (1971)

APPENDIX B

EXPERIMENTAL APPARATUS

The high speed photographic equipment used for investigating bubble dynamics will be described here. A schematic of the setup is shown in Figure B-1. The main components of the system are the laser, microscope, TV receiver and video recorder, pulse generators and control box. Basically the laser light passes through the sample and the image of the domains from the TV receiver are recorded on tape by the video recorder. The control box adjusts the relative timing of the light pulses and the field pulses moving the domains. The equipment can be used in two modes, 1-transmission (Faraday) mode where light passes through the sample, 2- reflection (Kerr) mode where light is reflected from the surfaces of the sample. Unless otherwise stated, it is understood below that the setup is in the transmission mode.

The light source of the system is a pulsed laser pumping a dye laser. The pulsed laser is a triggerable flowing nitrogen laser (Avco Everett Model C950A). Its output light flash is in the ultraviolet (3371$\mathring{A}$) and its bandwidth is less than 1$\mathring{A}$. It has an output peak power of 100 KW for 10 nsec duration. It can be externally triggered up to 200 Hz. The output of the pulsed laser is focused by a lens

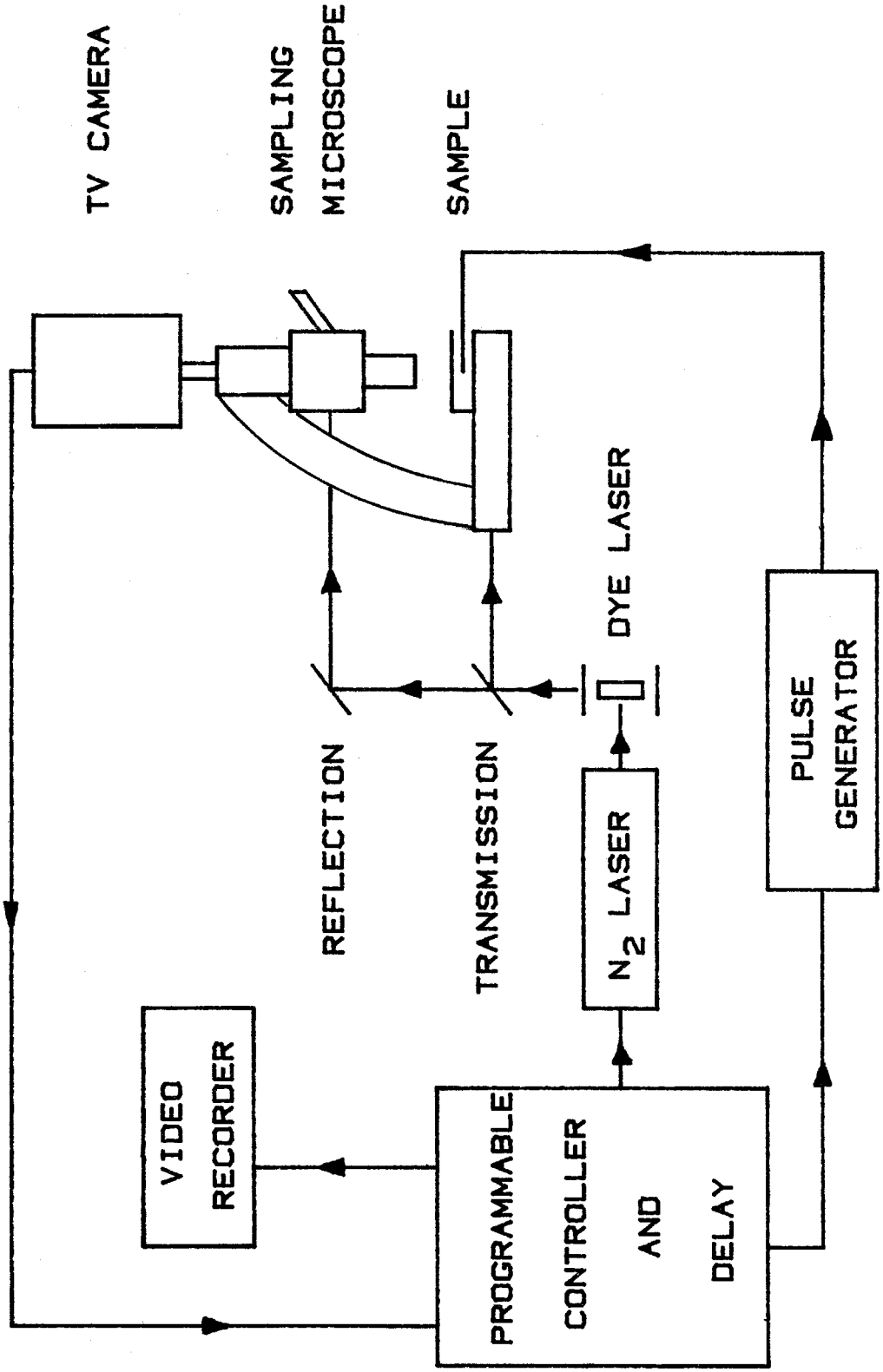

B.1. Block diagram of the optical sampling system

onto a Rhodamine 6G dye laser with a non-circulating dye cell. Rhodamine 6G is a stable and high output dye with an output wavelength of 5800 $\mathring{A}$. At this frequency the figure of merit (Faraday rotation/absorption) for garnets is high. The output peak power is reduced to 1.5 KW. Due to the short coherence length of the dye laser the problem of speckle is reduced.

A polarizing microscope (Leitz Ortholux-Pol) with most of its lenses removed is used for observing the domains. The pulsed laser light goes through the condenser lens, sheet polarizer, magnetic film, objective lens (x32/0.3-14 mm working distance), sheet analyzer and eyepiece (x 10), respectively. The domains are distinguished from one another by rotating the analyzer with respect to the polarizer. This way the domains can be made light or dark via the Faraday effect, depending on which direction they are oriented.

The domains are imaged onto a silicon intensified-target (SIT) of a Cohu 4400 Series TV camera and recorded on tape by a stop-motion video recorder. The SIT-TV camera increases sensitivity by about a factor of 100 over visual observation. It allows good image quality even when the light intensity levels are low (e.g., when the polarizer and analyzer are crossed or the magnification is high). The

10 nsec long laser flash generates an image on the SIT and the TV camera scans through it in 1/60th of a second. The contrast of the image is less in the following scans if the laser is not flashed again. The repetition rate of the laser is synchronized with the end of the TV scan. The images as well as digital information about the experiment (e.g., time, magnitude of applied fields, etc.) is recorded on video tape by a video recorder. The recorder is stop motion type allowing each recorded frame to be analyzed individually. Measurements on bubbles as well as digital information about each frame are obtained from the TV screen electronically and stored in cassettes by an HP-9821 computer.

The control box allows 32 step programming capability in the triggering orders of the laser flash and field pulses as well as letting the time delay between them. The repetition role of the laser can be adjusted to 7 1/2, 15, 30 or 60 Hz such that it flashes at the end of the TV scan. The delay between the laser flash and field pulses can be up to 10 μsecs. The delay can be changed manually or automatically. A fast silicon planar PIN photodiode (HPA5082-420) is used to detect the time when the laser flashes and its output goes to the delay circuit of the control box. The sampling interval (i.e., the time delay between successive

laser flashes) can be set from 0.25 nsecs up to 20 nsecs. All the information from the control box, such as the time, applied field magnitudes, frame numbers, codes, etc. are recorded digitally at the bottom of each video frame.

The applied fields are generated by various coils. The field pulses for bubble dynamics are supplied by a small (1 mm inner diameter) 10-turn pancake coil positioned close to the magnetic film. It has a negligible inductance and a calibration constant of 50 Oe/amp. HP-214A pulse generators (2 amps each into 50Ω) with a 7 nsec risetime each are used to drive the pancake coil and field pulses up to 300 Oe with a risetime of 20 nsec can be obtained this way. The field is uniform within 1.5% over the viewing area of 100 μms. Static bias fields normal to the sample up to 200 Oe are supplied by a 200-turn, 4 cm inner diameter, 8 cm outer diameter and 2.5 cm deep coil with the sample in the middle of the coil. The calibration constants of both the pancake coil and the bias field coil are obtained using the known collapse field of a sample. The static in-plane field is supplied by two large coils 16 cm apart, 10 cm inner diameter, 35 cm outer diameter, 6 cm deep and the sample is situated in the middle of the line joining their centers. The field up to 450 Oe magnitude

is calibrated by a Hall effect magnetometer and it is uniform to within 2% over the sample. The small unwanted bias field (4 Oe at 400 Oe in-plane field) generated by the in-plane field coils can be found and compensated by doing bubble collapse with the in-plane field in one direction and then in the opposite direction. The difference between the average of the two and the collapse field in either direction will give the magnitude of the extra bias field.

The setup can be used in the reflection (Kerr) mode also. Here light is reflected from the surfaces of the sample enabling domain wall dynamics at the surfaces to be investigated using the Kerr effect. In this mode the laser light is guided through the top of the microscope as shown in Figure B-1 and reflected perpendicular from the sample. There is no condenser lens and the laser light goes through the sheet polarizer, half silver mirror, x32 objective lens, is reflected from the sample and goes back through the x32 objective, half silver mirror again and the analyzer striking the SIT. The dye used in the dye laser for this mode is Coumarin 460 (7D4MC) and the output wavelengths is 4570 A (blue), shorter than the wavelength used for the transmission mode. This frequency gives the highest Kerr

rotation and least amount of light transmission through the sample so that domains are readily observable. The general quality of contrast is inferior to the transmission mode and only special (Bi-containing) samples can be used in this mode for surface studies. The other details of the setup are the same as in the transmission mode.

APPENDIX C

MATERIAL CHARACTERISTICS

The characteristics of the garnet materials used in the experiments are shown in Table C-1. The thickness of the films is measured by optical interferometry. The characteristic length ℓ and saturation magnetization $4\pi M_s$ are measured from the static bubble collapse field and bubble size measurements. The anisotropy field H_k, gyromagnetic ratio γ and the Gilbert damping constant are measured by ferromagnetic resonance (FMR). Only the bismuth containing sample, H280 had a high enough specific rotation and optical transmission that changed rapidly enough with wavelength to allow observation in the Kerr mode. The FMR spectra for this sample had multiple resonances so that only static bubble measurements were made. The samples are as-grown and their compositions are as follows: 2-16-44 ($Y_{1.57}Eu_{0.78}Tm_{0.65}Ge_{1.05}Fe_{3.95}O_{12}$), Un-335($Y_{2.45}Eu_{0.55}Ga_{1.2}Fe_{3.8}O_{12}$), 3-10-49($Y_{1.1}Eu_{0.6}Tm_{0.3}Ga_{1.15}Fe_{3.85}O_{12}$), LPED-252($Y_{2.35}Eu_{0.65}Ga_{1.09}Fe_{3.91}O_{12}$). The composition of the bismuth containing sample is not known.

SAMPLE	2-16-44	Un 335	3-10-49	LPED-252	H280
$\gamma(Oe^{-1}sec^{-1})x10^{-7}$	1.1	1.3	1.3	1.4	-
$H_k(Oe)$	3082	1070	2161	900	1443
α	0.026	0.035	0.029	0.035	-
$4\pi M(Oe)$	185	120	181	201	176
$h(\mu m)$	6.8	14	5.8	7.6	4.5
$\ell(\mu m)$	0.87	0.74	0.76	0.47	0.73

Table C.1. Material parameters of the garnet films